

## Tuning organic/inorganic interfaces via kinetic trapping, a case study

Anna Werkovits, Andreas Jeindl, Lukas Hörmann, Johannes Cartus, Oliver T. Hofmann

**Institute of Solid State Physics, TU Graz, NAWI Graz, Petersgasse 16/II, 8010 Graz, Austria.**

*Properties of inorganic-organic interfaces, such as their interface dipole, strongly depend on the structural arrangements of the organic molecules. A prime example is TCNE on Cu(111), which shows two different phases with a significant work function difference. However, the thermodynamically preferred phase is not always the one that is best suited for a given application. Rather, it may be desirable to selectively grow a kinetically trapped structure. In this work, we employ density functional theory and transition state theory to predict under which conditions such a kinetic trapping is possible for the model system of TCNE on Cu. In detail, we want to trap the molecules in the first layer in a flat-lying orientation. This requires suppressing the re-orientation to upright-standing TCNE that becomes thermodynamically more favorable for high dosages, while still enabling ordered growth. Based on the temperature-dependent diffusion and re-orientation rates, we propose a temperature range at which the re-orientation can be successfully suppressed.*

### I. INTRODUCTION

Metal-organic interfaces act as basis for a variety of possible nanotechnological applications, such as molecular switches,<sup>1,2</sup> thermoelectrics,<sup>3,4</sup> memories,<sup>5</sup> transistors,<sup>6–8</sup> or spintronic devices.<sup>9</sup> Due to the advances in computational material design, possibilities for developing functional interfaces with tailored physical properties and functionalities have increased in the last decades.<sup>10</sup> However, the functionality of these interfaces does not depend on the choice of the metal and the organic component alone. Rather, also the structure the organic component assumes on the surface plays a decisive role. A prime example are molecular acceptors that undergo a (coverage-dependent) re-orientation from flat-lying to upright-standing positions, like hexaazatriphenylene-hexacarbonitrile (HATCN) and dinitropyrene-tetraone (NO<sub>2</sub>-Pty) on Ag(111).<sup>11,12</sup> Because the electron affinity of organic films depends on their orientation,<sup>13</sup> this is accompanied by significant changes of the charge transfer and interface work functions.<sup>12,14</sup> In the two examples above, the structural transition causes a change of the work function of more than 1 eV, illustrating how important control over the structure is.

In principle, such a control can be achieved by identifying process conditions that allow to grow the target structure in thermodynamic equilibrium.<sup>15,16</sup> In practice, however, often kinetically trapped phases appear, especially when preparing interfaces using physical vapor deposition.<sup>17</sup> This is because kinetics plays a major role: Following Ostwald's rule of stages,<sup>18</sup> thermodynamically less stable structures form first. Whether the transition to a more stable structure occurs or whether the structure gets kinetically trapped depends on the energetic barriers and the corresponding transition rates. Therefore, we can make a virtue out of a necessity by explicitly utilizing kinetic trapping to grow structures out of thermodynamical equilibrium as well: In theory, controlled formation of a kinetically trapped structure should be possible by selecting a deposition temperature where the rate for the phase

transition to a thermodynamically more stable structure is slower than the speed at which the trapped structure grows. This requires profound knowledge of a) the underlying transition mechanisms, and b) the ability of the molecules to diffuse and aggregate, i.e. to form a seed for a different structure vis-à-vis to continue growing in the less thermodynamically stable form.

In this work, we perform a first step to predict controlled growth of the model system TCNE on Cu(111). While being computationally more tractable than its cousins HATCN and NO<sub>2</sub>-PyT on Ag(111), its manifold of possible structures reveals an even larger change in work function. When increasing the dosage of TCNE, the system undergoes a re-orientation from flat-lying to upright-standing molecules,<sup>19</sup> which leads to a work function increase of approximately 3 eV. When continuing growth, a second layer of TCNE forms on top of the first, standing, monolayer.<sup>19</sup> As the lowest deposited layer is the main influence for the properties of the interface,<sup>7</sup> e.g. the work function, it is highly interesting how the re-orientation of the first layer can be suppressed for high dosage.

However, computing TCNE on Cu(111) faces a fundamental challenge: The re-orientation on the surface substantially alters the way the molecules interact with the surface.<sup>19</sup> This includes charge transfer and the connected re-hybridization of molecular and metal orbitals. These orbital re-hybridizations are not covered by state-of-the-art force field-approaches, rendering them inapplicable here. Thus, we here use dispersion-corrected density functional theory (for details see Methods), despite the much larger computational cost compared to force fields.

Arguably, the ability of the system to undergo a phase transition depends on the molecules' ability to diffuse on the surface and, more importantly, on the rate at which they can change their orientation. Consequently, the first step is to investigate these processes for individual molecules rather than directly studying transitions between full close-packed structures. This is justified because both, the most favorable flat-lying and the most favorable upright-standing structure, consist of molecular geometries that would also be stable on their own (at least for very low temperatures) due to the strong molecule-substrate interactions. In addition, this reduced complexity enables studying kinetic processes at feasible cost.

Therefore, we omit multi-molecule processes that include intermolecular interactions, such as the initial nucleation, attachment and detachment processes from an island, and Ehrlich-Schwoebel barriers. Instead, we focus exclusively on two fundamental aspects in the low coverage growth regime: The diffusion and the re-orientation of individual molecules on the surface. In detail, minimum energy paths and transition states are obtained by the nudged elastic band method.<sup>20,21</sup> This method was previously successfully employed to study intramolecular reactions at inorganic-organic interfaces, like the cis-trans isomerization of azobenzene-derivates<sup>2,22</sup> induced by light, thermal energy, or STM pulses. Applying harmonic Transition State Theory,<sup>23,24</sup> we can further determine temperature-dependent rates of diffusion and re-orientation. This allows us to estimate a temperature range at which the re-orientation is suppressed while further growth of lying seeds is still supported - resulting in a kinetic trapping of lying TCNE.

## II. RESULTS AND DISCUSSION

### A. Transition paths and barriers

Before we explain which transitions we compute in detail, we briefly introduce the stable adsorption geometries of individual TCNE molecules on Cu(111) and the two structures we are interested in. This information was previously provided by Egger et. al.<sup>19</sup> and is repeated here for the sake of making the paper self-contained. The most favorable way for individual TCNE molecules to adsorb on the Cu(111) surface is in a “flat-lying” position. For this case, there are two different possible adsorption geometries (i.e., local minima) for the molecule, which we will further denote as  $L_1$  and  $L_2$  (see Figure 1). There are also four “upright-standing” adsorption geometries, denoted as  $S_1$  to  $S_4$ . Their energies are more than 0.3 eV higher, i.e. less stable.

In a full monolayer, at low coverages the energetically most favorable structure consists exclusively of flat-lying molecules in the  $L_1$  position, while its pendant for high coverages includes the upright-standing positions  $S_1$ ,  $S_3$  and  $S_4$  (for details see Supporting Information).<sup>19</sup> It is clear that for the flat-lying structure to grow, it is necessary that lying molecules can diffuse on the surface (“lying diffusion”). The formation of the upright standing structure requires that molecules can re-orient from lying to standing (“re-orientation”), and, potentially, that the standing molecules can also diffuse on the surface (“standing diffusion”).

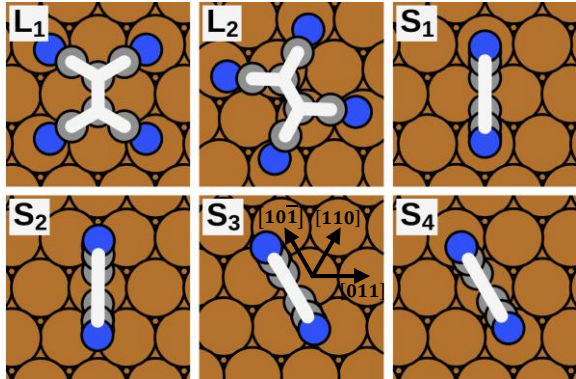


Figure 1: Top view of stable adsorption geometries for TCNE on Cu(111).<sup>19</sup> The orange spheres represent the Cu atoms of the substrate, whereas the grey and blue spheres are the C and N atoms, respectively. The white overlay is a reduced representation used in further plots. In addition, the directions of the Cu(111) substrate are provided.

To study diffusion and re-orientations, we create a representative set of distinct transitions between pairs of adsorption geometries (including rotational and translational symmetry equivalents). When naïvely accounting for e.g. three rotational and three translational symmetry equivalents for each adsorption geometry, we would already get  $\binom{36}{2} = 630$  transitions. Nevertheless, these will decompose into a manageable set of symmetry equivalent “elementary” transitions, i.e. transitions that possess exactly one transition state and therefore proceed in a single step. By knowing these elementary transitions, pathways can be constructed by linking individual elementary paths in a way that yields the lowest energetic barrier for the total transition. To efficiently obtain the most

relevant elementary transitions, sets of start- and endpoints are selected based on two concepts: Firstly, we restrict the selection to adsorption geometries in adjacent adsorption sites (i.e. translationally equivalent adsorption positions which are anchored on neighboring Cu atoms on the surface), implying that the adsorbate centers are at maximum one Cu-lattice constant apart. In other words, we neglect so called “long jumps”. This is warranted because there is evidence that such long jumps are improbable for moderate to low temperatures and for small molecules.<sup>25,26</sup> Secondly, we assume that for moderate to low temperatures kinetics is mainly dominated by transitions including the adsorption geometry with the lowest energy in its class either as start and/or end point (i.e. geometry **L**<sub>1</sub> for flat-lying adsorbates and **S**<sub>1</sub> for the upright-standing ones). This is warranted because low-energy structures also tend to have low-energy barriers due to their wide basin of attraction.<sup>27-30</sup> In hindsight, this assumption is also confirmed by our results (see below). Therefore, we initialized ten transitions as depicted in Figure 2 (a-j). Although we do not provide all possible transitions, with this strategy we expect to obtain the most dominant and thus limiting processes of the distinct transition regimes. To conveniently indicate transitions from an adsorption geometry **A** to another adsorption geometry **B**, we use a notation of the form **A**→**B**. Hereby, **A**→**B** is simply referred to as “forward” transition, while the transition with inverted initial and final states (**B**→**A**) is denoted as “reverse” transition.

To model the diffusion of lying TCNE molecules, we consider four possible transitions: Three different transitions that go directly from one **L**<sub>1</sub> to another **L**<sub>1</sub> at a different adsorption site (Figure 2a-c), and the transition from **L**<sub>1</sub> to the nearest **L**<sub>2</sub> geometry (Figure 2d). The different **L**<sub>1</sub>→**L**<sub>1</sub> transitions consist of two direct transitions to neighboring adsorption sites (shown in Figure 2a and b) and one transition to a symmetry-equivalent rotated geometry (Figure 2c).

For the re-orientation, we consider transitions from the lying minimum **L**<sub>1</sub> to the standing end points **S**<sub>1</sub> (Figure 2e), **S**<sub>3</sub> (Figure 2f) and **S**<sub>4</sub> (Figure 2g), i.e. to each of the geometries contained in the upright-standing structure.

For the diffusion of standing molecules, the most favorable adsorption geometry of this class, i.e. **S**<sub>1</sub>, is always contained as initial minimum that transitions into either **S**<sub>2</sub> (Figure 2h), **S**<sub>3</sub> (Figure 2i) or **S**<sub>4</sub> (Figure 2j). We note in passing that we have not explicitly included variants of the **S**<sub>1</sub>→**S**<sub>1</sub> in Figure 2. Rather, we found indications that the upright-standing diffusions of **S**<sub>1</sub> to all symmetry equivalent **S**<sub>1</sub> in adjacent adsorption sites (e.g. along the directions <011>) occur as multistep processes over **S**<sub>2</sub>, **S**<sub>3</sub> and/or **S**<sub>4</sub> (see Supporting Information).

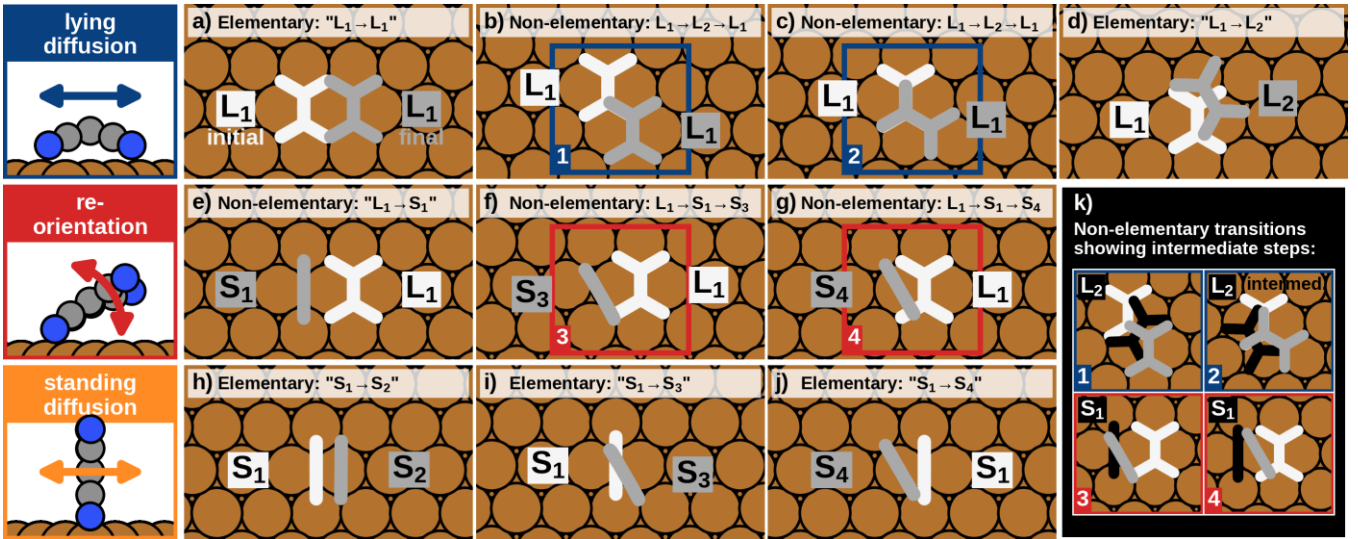
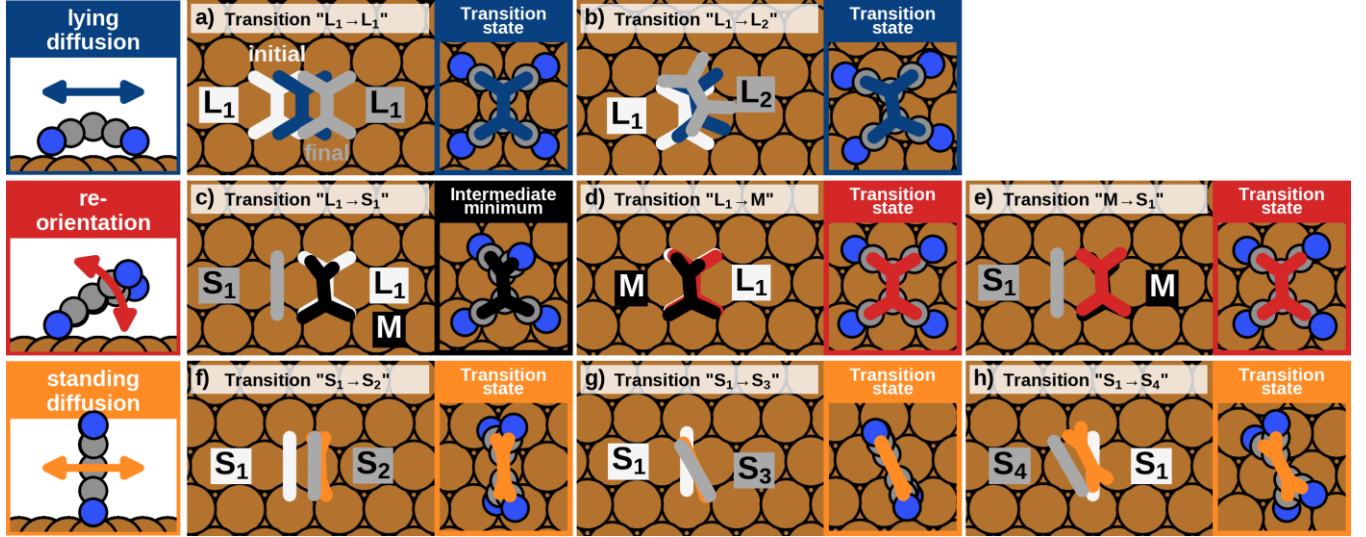


Figure 2: Start- and endpoints of the transitions for the lying diffusion (a-d), re-orientation (e-g) and the standing diffusion (h-j). For a clear representation, the molecule geometries are displayed in a reduced form that omits the nitrogen atoms, corresponding to the overlay in Figure 1. In (k), intermediate steps of multistep transitions (“non-elementary transitions”), of (b-c, f-g) are shown. All other transitions are investigated in detail and denoted by the label given in the subfigure captions, e.g.  $L_1 \rightarrow S_1$ .

In the course of our computations, we found that four of the ten initialized transitions occur as multi-step processes as they include another adsorption geometry and are therefore a combination of other transition processes: Two of the three  $L_1 \rightarrow L_1$  diffusion transitions (Figure 2b, c) proceed via the adsorption geometry  $L_2$  and thus reduce to consecutive transitions of  $L_1 \rightarrow L_2$  and  $L_2 \rightarrow L_1$  (Figure 2d). Therefore, the remaining  $L_1 \rightarrow L_1$  transition (Figure 2a) uniquely denotes the direct transition. In addition, the re-orientations  $L_1 \rightarrow S_3$  (Figure 2f) and  $L_1 \rightarrow S_4$  (Figure 2g) proceed via  $S_1$ , inferring that the main re-orientation process is  $L_1 \rightarrow S_1$  (Figure 2e). By investigating  $L_1 \rightarrow S_1$  in more detail (discussed later), we also found that this transition proceeds via a hitherto overlooked intermediate minimum (**M**). All remaining transitions occur as single step and possess exactly one transition state, i.e. “elementary” transitions. In total, the transition states (TS) and minimum energy paths of seven elementary transitions were obtained: Lying TCNE molecules can either diffuse along  $\langle 011 \rangle$  directions ( $L_1 \rightarrow L_1$ ) or perform rotations ( $L_1 \rightarrow L_2$ ). To overcome the barriers efficiently in a lying position, the adsorption height of the nitrogen atoms increases by up to 0.4 Å and the bending, which is favorable at the local adsorption geometries, reduces. The observed process of re-orientation from a flat-lying to an upright-standing position occurs consecutively via  $L_1 \rightarrow M$  and  $M \rightarrow S_1$ , as discussed later in more detail. For the standing diffusion, the motion in straight lines perpendicular to the molecular plane (similar to a walking motion) is enabled via  $S_1 \rightarrow S_2$ , while rotation between the directions  $\langle 011 \rangle$ ,  $\langle 110 \rangle$  and  $\langle 10\bar{1} \rangle$  of the Cu(111) surface occurs by  $S_1 \rightarrow S_3$  and  $S_1 \rightarrow S_4$ . For more insight, animated GIFs and geometry files are provided in the Supporting Information. Figure 3 shows an overview containing the main geometric characteristics. This includes the initial and final adsorption geometries, as well as the positions and the explicit geom-

tries of the obtained transition states. The only exception is the transition  $L_1 \rightarrow S_1$  (Figure 3c), where the intermediate minimum **M** is provided instead. The corresponding energy barriers, as well as the absolute adsorption energies of the initial states, the transition states and the final states are summarized in Table 1 and visualized in Figure 4. The detailed energy paths of all transitions are visualized in the Supporting Information.



**Figure 3:** Overview of the elementary transition processes of the three different motion regimes “lying diffusion” (a,b), “re-orientation” (c-e) and “standing diffusion” (f-h). In addition to the initial (white) and final (grey) adsorption geometries the positions of the transition states including their specific geometries are provided as well, except for  $L_1 \rightarrow S_1$  (c), where instead the obtained intermediate minimum “M” (black) is shown. The relative positions during the transitions itself are presented in a reduced scheme by omitting the nitrogen atoms.

**Table 1:** Energetics of the elementary transitions: Adsorption energies of the initial ( $E^{ini}$ ), transition ( $E^\ddagger$ ) and final state ( $E^{fin}$ ) and the corresponding barriers of the forward ( $\Delta E_1^\ddagger$ ) and the reverse ( $\Delta E_{-1}^\ddagger$ ) transition.

| Transition            | $E^{ini}$ / eV | $E^{fin}$ / eV | $E^\ddagger$ / eV | $\Delta E_1^\ddagger$ / eV | $\Delta E_{-1}^\ddagger$ / eV |
|-----------------------|----------------|----------------|-------------------|----------------------------|-------------------------------|
| $L_1 \rightarrow L_1$ | -2.04          | -2.04          | -1.80             | 0.24                       | 0.24                          |
| $L_1 \rightarrow L_2$ | -2.04          | -2.02          | -1.81             | 0.23                       | 0.21                          |
| $L_1 \rightarrow M$   | -2.04          | -1.94          | -1.87             | 0.17                       | 0.06                          |
| $M \rightarrow S_1$   | -1.94          | -1.73          | -1.69             | 0.25                       | 0.04                          |
| $S_1 \rightarrow S_2$ | -1.73          | -1.67          | -1.64             | 0.09                       | 0.03                          |
| $S_1 \rightarrow S_3$ | -1.73          | -1.63          | -1.62             | 0.11                       | 0.01                          |
| $S_1 \rightarrow S_4$ | -1.73          | -1.62          | -1.60             | 0.12                       | 0.01                          |

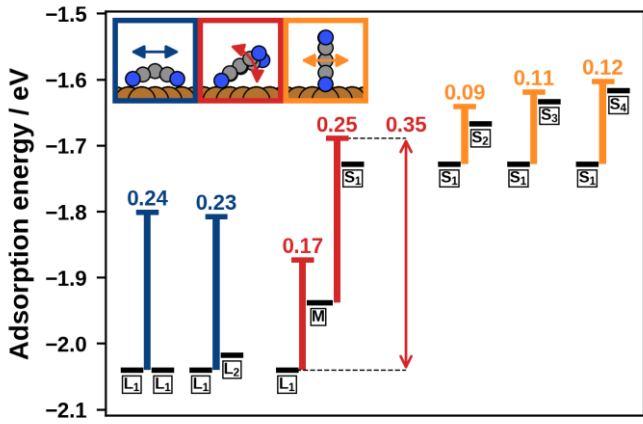


**Figure 4:** Adsorption energies of initial geometries, transition states, and final geometries of the various transitions. The black bars represent the energies of the local minima whereas the colored bars represent the energy barriers of the forward transitions. The arrow denotes the effective barrier for re-orienting from lying to standing TCNE.

Since the  $L_1 \rightarrow S_1$  re-orientation process will strongly determine the phase-transition versus growth behavior, it is useful to discuss this process in more detail. The computed minimum energy path, together with a set of characteristic adsorbate geometries, is visualized in Figure 5. As mentioned above, one can clearly see that this is a two-step process. The intermediate minimum **M** is 0.10 eV energetically less beneficial than  $L_1$ . The barrier of  $L_1 \rightarrow M$  is 0.17 eV, and thus smaller than the barrier of  $M \rightarrow S_1$ , which amounts to 0.25 eV. The effective total barrier for standing up, i.e. the difference between the lowest ( $L_1$ ) and highest point (transition state  $\ddagger_B$  in Figure 5) of the pathway, is 0.35 eV. For the reverse transition the molecule needs to overcome only a minute barrier of 0.04 eV between  $S_1$  and **M**. The backward reaction is completed by overcoming the barrier between **M** and  $L_1$  (0.06 eV)

In geometric terms, the re-orientation proceeds as follows: The lying TCNE detaches one CN-group, hereafter referred to as “arm”, from the surface before reaching the first transition state ( $\ddagger_A$ ). The molecule gains stability again at the intermediate minimum (**M**) by repositioning its opposite arm from the top to the hollow site. After the arm next to the already detached one breaks the second CN-Cu bond, both detached arms come closer to each other, until arriving at the second transition state ( $\ddagger_B$ ). Here the now nearly flat molecule encloses an angle of approximately 30° with the substrate surface. By rotating further into an upright position, the adsorption geometry  $S_1$  is reached. The two nitrogen atoms, which remain bound to the surface during the whole re-orientation process, move only slightly (0.4 Å in the lateral and -0.2 Å in the vertical direction).

It is likely that the re-orientation process of  $L_2 \rightarrow S_4$  follows a similar pathway. However, this transition cannot be rate-limiting for the targeted kinetic trapping, because the difference of the adsorption energies of  $L_2$  and  $S_4$  (0.40 eV) is already larger than the barrier of  $L_1 \rightarrow S_1$  (0.35 eV).

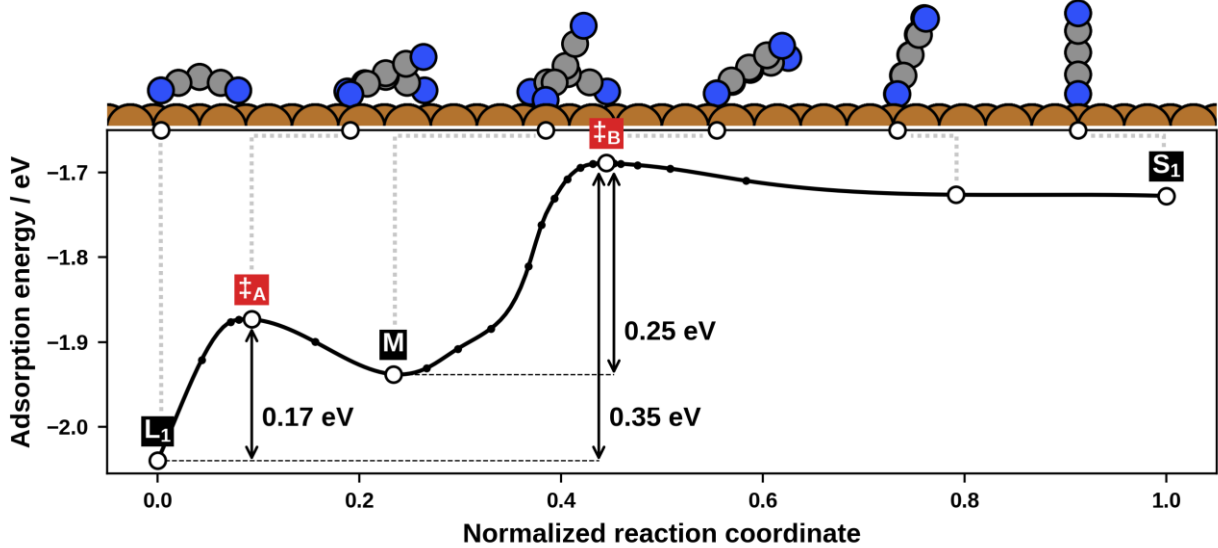


**Figure 5:** Energy evolution while re-orientating from flat-lying to upright-standing position. Geometries of characteristic positions are provided in the side view for the initial ( $L_1$ ), intermediate ( $M$ ) and final ( $S_1$ ) minima, as well as the two transition states  $\ddagger_A$  and  $\ddagger_B$ .

### B. Transition rates

To determine under which conditions the re-orientation of TCNE molecules can be prevented, while still allowing for growth of the flat-lying structures, we need to obtain temperature-dependent transition rates by utilizing the energy barriers. We assume that in a hypothetical physical vapor deposition (PVD) experiment an ordered flat-lying structure can form as long as the temperature is sufficiently high for the molecules to readily diffuse. The speed at which this structure grows is then limited by the available material. In a PVD experiment, this is given by the rate at which TCNE molecules are deposited onto the substrate. Furthermore, it is plausible to assume that the structure becomes (kinetically) stabilized once it reaches mesoscopic dimensions or becomes buried under a significant amount of material, i.e. once the deposited TCNE is several layers thick. In other words, if the growth to multilayers occurs faster than the time required for even a single TCNE to re-orient into an upright position, we assume to have kinetically trapped the flat-lying structure. In short, we need to find a temperature range where a) diffusion of molecules is much faster and b) the re-orientation is slower than a given deposition rate.

We can calculate temperature-dependent transition rates  $k(T)$  utilizing the harmonic transition state theory (see Methods for details) with energy barriers  $\Delta E^\ddagger$  from Table 1 and attempt frequencies  $A$ , as provided in Table 2:

$$k(T) = A e^{-\frac{\Delta E^\ddagger}{k_B T}} \quad (\text{Equation 1})$$

Since our goal is to prevent the re-orientation of individual molecules to the upright-standing position, we want to discuss a joint process of the re-orientation ( $L_1 \rightarrow S_1$ ) rather than the separate elementary transitions  $L_1 \rightarrow M$  and

**M → S<sub>1</sub>**. Thus, we assign an effective barrier of 0.35 eV to the joint process of standing up. The rate-limiting step of the lying down is **M → L<sub>1</sub>**, with a barrier of 0.06 eV.

The crucial aspect for the rates, beyond the energy barriers, are the attempt frequencies of the transitions. In principle, attempt frequencies are the vibration frequencies in direction of the reaction coordinate. Within harmonic transition state theory, they are explicitly obtained from the stable vibration frequencies of the initial and the transition states (for details see Methods). As Table 2 shows, the attempt frequencies are very different for different processes, covering four orders of magnitude. The **S<sub>1</sub> → S<sub>3</sub>** transition of the standing diffusion has the lowest attempt frequency (with  $1.0 \times 10^{12}$  Hz), while the largest attempt frequency is obtained for the **L<sub>1</sub> → L<sub>1</sub>** diffusion with  $2.0 \times 10^{15}$  Hz. In total, attempt frequencies for the lying diffusion are by up to three orders of magnitude larger than the ones of the standing diffusion. For the re-orientation process, attempt frequencies of the standing-up are at least ten times larger than the attempt frequencies of falling-over.

**Table 2:** Attempt frequencies obtained by means of harmonic transition state theory. The subscripts 1 and -1 denote forward and reverse transitions, respectively.

|                            | <b>L<sub>1</sub> → L<sub>1</sub></b> | <b>L<sub>1</sub> → L<sub>2</sub></b> | <b>L<sub>1</sub> → S<sub>1</sub></b> | <b>S<sub>1</sub> → S<sub>2</sub></b> | <b>S<sub>1</sub> → S<sub>3</sub></b> | <b>S<sub>1</sub> → S<sub>4</sub></b> |
|----------------------------|--------------------------------------|--------------------------------------|--------------------------------------|--------------------------------------|--------------------------------------|--------------------------------------|
| <b>A<sub>1</sub> / Hz</b>  | $2.0 \times 10^{15}$                 | $2.9 \times 10^{14}$                 | $5.0 \times 10^{13}$                 | $1.7 \times 10^{12}$                 | $1.0 \times 10^{12}$                 | $1.7 \times 10^{13}$                 |
| <b>A<sub>-1</sub> / Hz</b> | $2.0 \times 10^{15}$                 | $1.3 \times 10^{14}$                 | $9.0 \times 10^{12}$                 | $4.6 \times 10^{12}$                 | $1.2 \times 10^{12}$                 | $1.3 \times 10^{13}$                 |

Using these attempt frequencies, the temperature-dependent transition rates according to Equation 1 are calculated and shown in Figure 6. Before explicitly investigating the rates of the single processes, we discuss at which rates we can consider transitions to be suppressed within the growth process. Within PVD experiments, thin films (i.e., multilayers) of organic materials are typically deposited within minutes to (at most) days. This corresponds to deposition rates  $k_{\text{dep}}$  of about 1 monolayer per minute to 1 monolayer per day. Based on the obtained transition rates (Figure 6), we can identify at which temperatures individual processes occur on much longer time scales than the deposition process itself. In other words: We can consider single processes as suppressed if transition rates  $k < k_{\text{dep}}$  are enforced. For the present discussion, we propose a target transition rate  $k$  of 1 transition per day ( $10^{-5}$  transitions per second), as indicated by the black line. The temperatures required to reach this target transition rate are stated in Table 3. A detailed uncertainty discussion including root mean square uncertainty estimates of the obtained suppression temperatures is given in the Supporting Information. To summarize the outcome, we estimate the uncertainty of the suppression temperatures of the lying diffusion to  $\approx 15$  K, whereas the one for standing-up is with  $\approx 20$  K the largest error estimate. For all other transitions the uncertainty is below 10 K.

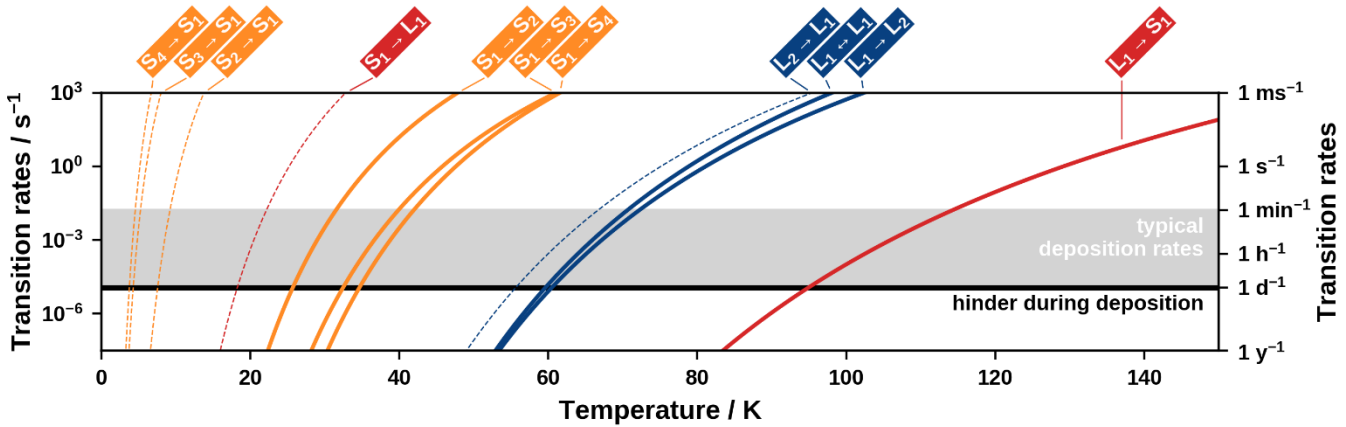


**Figure 6:** Transition rates as function of the process temperature. Forward transitions are plotted in solid lines, reverse transitions in dashed lines. In addition, the range of typical deposition rates is marked, as well as the limiting transition rate for hindering distinct processes during deposition.

**Table 3:** Estimated temperatures for suppression  $T$  computed for transition rates of 1 transition per day. The subscripts 1 and -1 refer to forward and reverse transitions, respectively.

|              | $L_1 \rightarrow L_1$ | $L_1 \rightarrow L_2$ | $L_1 \rightarrow S_1$ | $S_1 \rightarrow S_2$ | $S_1 \rightarrow S_3$ | $S_1 \rightarrow S_4$ |
|--------------|-----------------------|-----------------------|-----------------------|-----------------------|-----------------------|-----------------------|
| $T_1 / K$    | 60                    | 60                    | 95                    | 26                    | 32                    | 35                    |
| $T_{-1} / K$ | 60                    | 56                    | 18                    | 8                     | 4                     | 4                     |

In Figure 6, the transitions of standing molecules to the most stable standing geometry  $S_1$  (shown as dashed yellow lines) are the fastest processes. Similarly fast is the falling over of upright standing molecules ( $S_1 \rightarrow L_1$ , dashed red line). Both processes occur on sub-millisecond timescales for temperatures above 30 K. Next in line, we find the change of  $S_1$  molecules to energetically less favorable upright standing positions (solid yellow lines), which dominate the ability of diffusion in this orientation. Therefore, it is more probable for individual standing TCNE molecules to fall over again, than to diffuse over long distances in the standing orientation (at least for temperatures below room temperature). The diffusion of the flat-lying molecules (blue lines) occurs very quickly at temperatures above 100 K, but freezes out at temperatures below 55 to 65 K. Finally, the joint process of standing up ( $L_1 \rightarrow S_1$ ) is the slowest. It still occurs very efficiently at moderate temperatures (millisecond timescale at 140 K, and almost instantaneously at room temperature), but less than one transition per day occurs at temperatures as high as 95 K. Here, we remind the reader that this joint process is, indeed, a two-step process. For the sake of completeness, the rates for these two elementary processes are discussed in the Supporting Information.

Based on these results, we predict that, in the temperature range of 65 to 95 K, the standing-up of individual molecules can be suppressed while molecules can sufficiently diffuse in the lying orientation. When cooling the substrate with liquid nitrogen (77 K), lying molecules diffuse by a rate of  $\approx 0.2$  transitions per second. This should be sufficiently high to ensure a diffusion mobility that allows building at least a full lying monolayer within the

deposition time. For lower temperatures, growth of ordered structured will be inhibited by random aggregation of impinging molecules. For 77 K, the rate of standing-up is lower than one transition per year. Once they are standing, the molecules fall down again within a picosecond timescale. Therefore, it is very unlikely that standing seeds are created during the growth process and the distinct knowledge of the influence of standing seeds on the stability of standing molecules becomes dispensable.

For dosages that exceed the coverage of the favored flat-lying structure, i.e. when a second layer is created, we assume that the re-orientation of the whole monolayer can be suppressed as well for temperatures below 95 K. At higher dosages, the re-orientation rate will increase, but by depositing further layer fast enough until the layer thickness reaches a mesoscopic scale, we expect to prevent the re-orientation of the whole first layer. To check, whether this assumption holds true, detailed investigations about the intermolecular and interlayer processes will need to be performed in the future. This work constitutes a first step towards this goal of fully understanding transition processes of organic thin films.

### III. CONCLUSION

In summary, we studied kinetic processes of individual TCNE molecules on a Cu(111) surface to propose experimental conditions that prevent the thermodynamically favored re-orientation of the molecules in the first adsorbate layer from flat-lying to upright-standing positions. For this purpose, energy barriers and transition rates of single-molecule-processes (diffusion of lying and standing TCNE molecules, as well as the re-orientation between lying and standing) were determined via the nudged elastic band method and harmonic transition state theory. The most dominant and thus limiting re-orientation process turned out to advance in two steps while exhibiting an effective energy barrier of 0.35 eV. Based on the obtained rates, we estimate that for temperatures above 65 K a sufficiently high diffusion mobility is ensured, which further allows the formation of an ordered monolayer of flat-lying TCNE. At the same time, our results indicate that for temperatures below 95 K a monolayer can be kinetically trapped against re-orientation to an upright-standing structure by preventing re-orientation of the individual TCNE molecules. A full image on how long the first layer remains kinetically trapped upon deposition of further layers will require further studies on the intermolecular and interlayer processes.

### IV. METHODS

In this work, the sampling of the potential energy surface is conducted within the framework of Kohn-Sham density functional theory by using numeric atom-centered basis functions as implemented in the software package FHI-aims.<sup>31</sup> We use the PBE<sup>32</sup> functional and the TS<sup>surf</sup> dispersion correction.<sup>33</sup> All further numerical settings were converged to within 10 meV (see Supporting Information for details).

All calculations are performed with periodic boundary conditions on a slab with 7 copper layers with one TCNE adsorbate in a 4x4 super cell. The two uppermost layers of the copper substrate were pre-relaxed first, but kept fixed for all other calculations and optimizations, e.g. minimum search and transition state search. In contrast, all

atoms of the TCNE molecules were allowed to move freely (resulting in 30 degrees of freedom). The resulting energies correspond to electronic energies of the whole system  $E_{\text{sys}}$  at zero Kelvin. Adsorption energies  $E_{\text{ads}}$  are determined according to Equation 1, where  $E_{\text{mol}}$  is the energy of a relaxed molecule in the gas phase and  $E_{\text{sub}}$  the energy of the pre-relaxed substrate, as used in the slab.

$$E_{\text{ads}} = E_{\text{sys}} - E_{\text{mol}} - E_{\text{sub}} \quad (\text{Equation 2})$$

By this definition, more favored adsorption geometries are connected to more negative energies.

While molecular dynamics simulations are the standard method for kinetic studies, its application isn't affordable for the investigated system and purpose. As timesteps for similar systems are typically in the order of femtoseconds or less, the available simulation time is not sufficient for reliably escaping basins of a wide area of attraction to measure barriers and rates of e.g. processes like re-orientations. The computational cost is further increased by sampling the potential energy surface on the level of density function theory, which is necessary to capture the underlying chemistry. Even though advances in accelerating sampling of rare events<sup>34–36</sup> have been made, we decided on using transition path sampling methods instead. Transition rates between single adsorption minima are provided via harmonic transition state theory, whereas energy barriers themselves are determined beforehand with a transition state search method.

For the transition state search, the climbing image nudged elastic band (CI-NEB) method<sup>20,21</sup> augmented with the Fast Inertial Relaxation Engine (FIRE) optimizer<sup>37</sup> is applied. The workflow can be summed up as the following: The transition path is initialized between the selected pair of minima with up to five images using the image dependent pair potential (IDPP) method<sup>38</sup> as shipped by the software package ASE.<sup>39</sup> After several iterations, only the images with the highest energies and/or forces are updated for efficiency reasons. Once the NEB force of the image with the highest energy drops below 0.01 eV/Å, further images are inserted and converged to verify that the highest barrier along the path is found. All transition paths are sampled by 7 to 25 images with a maximum residual NEB force of 0.05 eV/Å, whereas the NEB forces of all transition states are below  $\approx 0.01$  eV/Å. The transition state is, per definition, a first order saddle point, where the Hessian exhibits exactly one unstable eigenmode that corresponds to a negative curvature or eigenfrequency.

Numerical vibrational analyses were performed (at the  $\Gamma$ -point) for all minima and transition states, in order to a) assure that the transition states have only one negative frequency, and b) to obtain the attempt frequencies required for the harmonic transition state theory. Displacements of 0.01 Å are applied for computing Hessians. In the Supporting Information, we explain why Hessians are symmetrized and how additional unstable frequencies at transition states and minima are treated.

The harmonic transition state theory<sup>23,24</sup> enables determining the transition rates  $k$  as stated in Equation 4.

$$k = A e^{-\frac{\Delta G^\ddagger}{k_B T}} \quad \text{with} \quad A = \frac{\prod_{i=1}^{3N} \nu_i^{\text{ini}}}{\prod_{i=1}^{3N-1} \nu_i^\ddagger} \quad \text{and} \quad \Delta G^\ddagger = G^\ddagger - G^{\text{ini}} \quad (\text{Equation 4})$$

Therein,  $k$  is the product of the harmonic attempt frequency  $A$  and the Boltzmann-factor containing the Gibbs free energy barrier  $\Delta G^\ddagger$  and the temperature  $T$ .  $\Delta G^\ddagger$  is the difference of the Gibbs free energy of the transition state (superscript  $\ddagger$ ) and the initial state (superscript ini), and in general also depends on the electronic energy, the temperature, the pressure and the unit cell size. In this study, however, the unit cell size and the number of adsorbate molecules per unit cell stays unchanged for all transitions which reduces the dependency of  $\Delta G^\ddagger$  to the pure electronic energy barrier  $\Delta E^\ddagger$  (see Supporting Information for details).  $A$  is the ratio of the products of the stable vibration frequencies  $\nu_i$  at the initial and the transition state.

## ASSOCIATED CONTENT

The Supporting Information is appended at the end of the manuscript.

## ACKNOWLEDGMENTS

We acknowledge fruitful discussions with F. Calcinelli, B. Ramsauer, R. Berger and R. Steentjes. Funding through the START project of the Austrian Science Fund (FWF): Y1175-N36 is gratefully acknowledged. Computational results have been achieved using the Vienna Scientific Cluster (VSC).

## REFERENCES

- (1) Katsonis, N.; Lubomska, M.; Pollard, M. M.; Feringa, B. L.; Rudolf, P. Synthetic Light-Activated Molecular Switches and Motors on Surfaces. *Progress in Surface Science*. 2007, pp 407–434. <https://doi.org/10.1016/j.progsurf.2007.03.011>.
- (2) McNellis, E.; Meyer, J.; Baghi, A. D.; Reuter, K. Stabilizing a Molecular Switch at Solid Surfaces: A Density Functional Theory Study of Azobenzene on Cu(111), Ag(111), and Au(111). *Phys. Rev. B - Condens. Matter Mater. Phys.* **2009**, *80* (3). <https://doi.org/10.1103/PhysRevB.80.035414>.
- (3) Paulsson, M.; Datta, S. Thermoelectric Effect in Molecular Electronics. *Phys. Rev. B - Condens. Matter Mater. Phys.* **2003**, *67* (24), 241403. <https://doi.org/10.1103/PhysRevB.67.241403>.
- (4) Reddy, P.; Jang, S. Y.; Segalman, R. A.; Majumdar, A. Thermoelectricity in Molecular Junctions. *Science (80-)*. **2007**, *315* (5818), 1568–1571. <https://doi.org/10.1126/science.1137149>.
- (5) Cho, B.; Song, S.; Ji, Y.; Kim, T.-W.; Lee, T. Organic Resistive Memory Devices: Performance Enhancement, Integration, and Advanced Architectures. *Adv. Funct. Mater.* **2011**, *21* (15), 2806–2829. <https://doi.org/10.1002/adfm.201100686>.
- (6) Veres, J.; Ogier, S.; Lloyd, G.; De Leeuw, D. Gate Insulators in Organic Field-Effect Transistors. *Chemistry of Materials*. November 16, 2004, pp 4543–4555. <https://doi.org/10.1021/cm049598q>.
- (7) Koch, N. Organic Electronic Devices and Their Functional Interfaces. *ChemPhysChem* **2007**, *8* (10), 1438–1455. <https://doi.org/10.1002/cphc.200700177>.
- (8) Virkar, A. A.; Mannsfeld, S.; Bao, Z.; Stingelin, N. Organic Semiconductor Growth and Morphology Considerations for Organic Thin-Film Transistors. *Adv. Mater.* **2010**, *22* (34), 3857–3875. <https://doi.org/10.1002/adma.200903193>.
- (9) Sanvito, S. Part of the Molecule-Based Magnets Themed Issue. *Chem. Soc. Rev.* **2011**, *40* (6), 3336–3355. <https://doi.org/10.1039/c1cs15047b>.
- (10) Goronzy, D. P.; Ebrahimi, M.; Rosei, F.; Arramel, A.; Fang, Y.; De Feyter, S.; Tait, S. L.; Wang, C.; Beton, P. H.; Wee, A. T. S.; Weiss, P. S.; Perepichka, D. F. Supramolecular Assemblies on Surfaces: Nanopatterning, Functionality, and Reactivity. *ACS Nano* **2018**, *12*, 30. <https://doi.org/10.1021/acsnano.8b03513>.

(11) Bröker, B.; Hofmann, O. T.; Rangger, G. M.; Frank, P.; Blum, R.-P.; Rieger, R.; Venema, L.; Vollmer, A.; Müllen, K.; Rabe, J. P.; Winkler, A.; Rudolf, P.; Zojer, E.; Koch, N. Density-Dependent Reorientation and Rehybridization of Chemisorbed Conjugated Molecules for Controlling Interface Electronic Structure. *Phys. Rev. Lett.* **2010**, *104* (24), 246805. <https://doi.org/10.1103/PhysRevLett.104.246805>.

(12) Hofmann, O. T.; Glowatzki, H.; Bürker, C.; Rangger, G. M.; Bröker, B.; Niederhausen, J.; Hosokai, T.; Salzmann, I.; Blum, R.; Rieger, R.; Vollmer, A.; Rajput, P.; Gerlach, A.; Müllen, K.; Schreiber, F.; Zojer, E.; Koch, N.; Duhm, S. Orientation-Dependent Work-Function Modification Using Substituted Pyrene-Based Acceptors. *J. Phys. Chem. C* **2017**, *121* (44), 24657–24668. <https://doi.org/10.1021/acs.jpcc.7b08451>.

(13) Duhm, S.; Heimel, G.; Salzmann, I.; Glowatzki, H.; Johnson, R. L.; Vollmer, A.; Rabe, J. P.; Koch, N. Orientation-Dependent Ionization Energies and Interface Dipoles in Ordered Molecular Assemblies. *Nat. Mater.* **2008**, *7* (4), 326–332. <https://doi.org/10.1038/nmat2119>.

(14) Glowatzki, H.; Bröker, B.; Blum, R. P.; Hofmann, O. T.; Vollmer, A.; Rieger, R.; Mullen, K.; Zojer, E.; Rabe, J. P.; Koch, N. “Soft” Metallic Contact to Isolated C<sub>60</sub> Molecules. *Nano Lett.* **2008**, *8* (11), 3825–3829. <https://doi.org/10.1021/nl8021797>.

(15) Lopez-Otero, A. Hot Wall Epitaxy. *Thin Solid Films* **1978**, *49* (1), 3–57. [https://doi.org/10.1016/0040-6090\(78\)90309-7](https://doi.org/10.1016/0040-6090(78)90309-7).

(16) Sitter, H.; Andreev, A.; Matt, G.; Sariciftci, N. S. Hot Wall Epitaxial Growth of Highly Ordered Organic Epilayers. *Synth. Met.* **2003**, *138* (1–2), 9–13. [https://doi.org/10.1016/S0379-6779\(02\)01306-1](https://doi.org/10.1016/S0379-6779(02)01306-1).

(17) Jones, A. O. F.; Chattopadhyay, B.; Geerts, Y. H.; Resel, R. Substrate-Induced and Thin-Film Phases: Polymorphism of Organic Materials on Surfaces. *Advanced Functional Materials*. Wiley-VCH Verlag April 12, 2016, pp 2233–2255. <https://doi.org/10.1002/adfm.201503169>.

(18) Ostwald, W. Studien Über Die Bildung Und Umwandlung Fester Körper. *Zeitschrift für Phys. Chemie* **2017**, *22U* (1), 289–330. <https://doi.org/10.1515/zpch-1897-2233>.

(19) Egger, A. T.; Hörmann, L.; Jeindl, A.; Scherbel, M.; Obersteiner, V.; Todorović, M.; Rinke, P.; Hofmann, O. T. Charge Transfer into Organic Thin Films: A Deeper Insight through Machine-Learning-Assisted Structure Search. *Adv. Sci.* **2020**, *7* (15), 2000992.

[https://doi.org/10.1002/advs.202000992.](https://doi.org/10.1002/advs.202000992)

(20) Henkelman, G.; Uberuaga, B. P.; Jónsson, H. A Climbing Image Nudged Elastic Band Method for Finding Saddle Points and Minimum Energy Paths. *J. Chem. Phys.* **2000**, *113*, 9901. <https://doi.org/10.1063/1.1329672>.

(21) Henkelman, G.; Jónsson, H.; Jó, H. Improved Tangent Estimate in the Nudged Elastic Band Method for Finding Minimum Energy Paths and Saddle Points. *J. Chem. Phys.* **2000**, *113*, 5648. <https://doi.org/10.1063/1.1323224>.

(22) Ferri, V.; Elbing, M.; Pace, G.; Dickey, M. D.; Zharnikov, M.; Samor, P.; Mayor, M.; Rampi, M. A. Light-Powered Electrical Switch Based on Cargo-Lifting Azobenzene Monolayers. *Angew. Chemie - Int. Ed.* **2008**, *47* (18), 3407–3409. <https://doi.org/10.1002/anie.200705339>.

(23) Eyring, H. The Activated Complex in Chemical Reactions. *J. Chem. Phys.* **1935**, *3* (2), 63–71. <https://doi.org/10.1063/1.1749604>.

(24) Vineyard, G. H. Frequency Factors and Isotope Effects in Solid State Rate Processes. *J. Phys. Chem. Solids* **1957**, *3* (1–2), 121–127. [https://doi.org/10.1016/0022-3697\(57\)90059-8](https://doi.org/10.1016/0022-3697(57)90059-8).

(25) Schunack, M.; Linderoth, T. R.; Rosei, F.; Lægsgaard, E.; Stensgaard, I.; Besenbacher, F. Long Jumps in the Surface Diffusion of Large Molecules. *Phys. Rev. Lett.* **2002**, *88* (15), 4. <https://doi.org/10.1103/PhysRevLett.88.156102>.

(26) Antczak, G.; Ehrlich, G. Long Jumps in Surface Diffusion. *J. Colloid Interface Sci.* **2004**, *276* (1), 1–5. <https://doi.org/10.1016/j.jcis.2003.11.035>.

(27) Liborio, L.; Sturniolo, S.; Jochym, D. Computational Prediction of Muon Stopping Sites Using Ab Initio Random Structure Searching (AIRSS). *J. Chem. Phys.* **2018**, *148* (13), 134114. <https://doi.org/10.1063/1.5024450>.

(28) Doye, J. P. K.; Wales, D. J.; Miller, M. A. Thermodynamics and the Global Optimization of Lennard-Jones Clusters. *J. Chem. Phys.* **1998**, *109* (19), 8143–8153. <https://doi.org/10.1063/1.477477>.

(29) Doye, J. P. K.; Massen, C. P. Characterizing the Network Topology of the Energy Landscapes of Atomic Clusters. *J. Chem. Phys.* **2005**, *122* (8), 104504. <https://doi.org/10.1063/1.1850468>.

(30) Massen, C. P.; Doye, J. P. K. Power-Law Distributions for the Areas of the Basins of Attraction on

a Potential Energy Landscape. *Phys. Rev. E - Stat. Nonlinear, Soft Matter Phys.* **2007**, *75* (3), 037101. <https://doi.org/10.1103/PhysRevE.75.037101>.

(31) Blum, V.; Gehrke, R.; Hanke, F.; Havu, P.; Havu, V.; Ren, X.; Reuter, K.; Scheffler, M. Ab Initio Molecular Simulations with Numeric Atom-Centered Orbitals. *Comput. Phys. Commun.* **2009**, *180* (11), 2175–2196. <https://doi.org/10.1016/j.cpc.2009.06.022>.

(32) Perdew, J. P.; Burke, K.; Ernzerhof, M. Generalized Gradient Approximation Made Simple. *Phys. Rev. Lett.* **1996**, *77* (18), 3865–3868. <https://doi.org/10.1103/PhysRevLett.77.3865>.

(33) Tkatchenko, A.; Scheffler, M. Accurate Molecular van Der Waals Interactions from Ground-State Electron Density and Free-Atom Reference Data. *Phys. Rev. Lett.* **2009**, *102* (7), 073005. <https://doi.org/10.1103/PhysRevLett.102.073005>.

(34) Shivpuje, S.; Jaipal, M.; Chatterjee, A. Accelerating Rare Events Using Temperature Programmed Molecular Dynamics: A Review. *Mol. Simul.* **2019**, *45* (14–15), 1295–1303. <https://doi.org/10.1080/08927022.2019.1619929>.

(35) Vandermause, J.; Torrisi, S. B.; Batzner, S.; Xie, Y.; Sun, L.; Kolpak, A. M.; Kozinsky, B. On-the-Fly Active Learning of Interpretable Bayesian Force Fields for Atomistic Rare Events. *npj Comput. Mater.* **2020**, *6* (1), 1–11. <https://doi.org/10.1038/s41524-020-0283-z>.

(36) Hartmann, C.; Banisch, R.; Sarich, M.; Badowski, T.; Schütte, C. Characterization of Rare Events in Molecular Dynamics. *Entropy* **2013**, *16* (1), 350–376. <https://doi.org/10.3390/e16010350>.

(37) Bitzek, E.; Koskinen, P.; Gähler, F.; Moseler, M.; Gumbsch, P. Structural Relaxation Made Simple. **2006**. <https://doi.org/10.1103/PhysRevLett.97.170201>.

(38) Smidstrup, S.; Pedersen, A.; Stokbro, K.; Jónsson, H. Improved Initial Guess for Minimum Energy Path Calculations. *J. Chem. Phys.* **2014**, *140*, 214106. <https://doi.org/10.1063/1.4878664>.

(39) Hjorth Larsen, A.; JØrgen Mortensen, J.; Blomqvist, J.; Castelli, I. E.; Christensen, R.; Dułak, M.; Friis, J.; Groves, M. N.; Hammer, B.; Hargus, C.; Hermes, E. D.; Jennings, P. C.; Bjerre Jensen, P.; Kermode, J.; Kitchin, J. R.; Leonhard Kolsbjer, E.; Kubal, J.; Kaasbjer, K.; Lysgaard, S.; Bergmann Maronsson, J.; Maxson, T.; Olsen, T.; Pastewka, L.; Peterson, A.; Rostgaard, C.; SchiØtz, J.; Schütt, O.; Strange, M.; Thygesen, K. S.; Vegge, T.; Vilhelmsen, L.; Walter, M.; Zeng, Z.; Jacobsen, K. W. The Atomic Simulation Environment - A Python Library for Working with Atoms. *Journal of Physics Condensed Matter*. Institute of Physics Publishing June 7, 2017, p 30.

<https://doi.org/10.1088/1361-648X/aa680e>.

# Supporting Information

for “Tuning organic/inorganic interfaces via kinetic trapping, a case study”

Anna Werkovits, Andreas Jeindl, Lukas Hörmann, Johannes Cartus, Oliver T. Hofmann

## Contents

|  |    |
|--|----|
| 1 Numerical settings of the DFT calculations.....              | 2  |
| 2 Favored monolayers.....                                      | 2  |
| 3 Transitions.....   | 3  |
| 3.1 $S_1 \rightarrow S_1$ transition.....                      | 3  |
| 3.2 Elementary transitions.....                                | 4  |
| 4 Transition Rates .....                                       | 5  |
| 4.1 Treatment of the Gibbs free energy .....                   | 5  |
| 4.2 Elementary transitions of the re-orientation process ..... | 5  |
| 4.3 Joint process of re-orientation.....                       | 6  |
| 5 Uncertainty discussion .....                                 | 7  |
| 5.1 Transition states and energy barriers .....                | 7  |
| 5.2 Vibration frequencies.....                                 | 8  |
| 5.2.1 Asymmetry .....  | 8  |
| 5.2.2 Quality of transition states and minima .....            | 8  |
| 5.2.3 Uncertainty estimation of vibrational frequencies.....   | 11 |
| 5.3 Attempt frequencies .....                                  | 12 |
| 5.4 Suppression temperatures.....                              | 12 |
| 6 References.....  | 14 |

## 1 Numerical settings of the DFT calculations

All DFT calculations are conducted with the software package FHI-aims<sup>1</sup> using PBE<sup>2</sup> as exchange correlational functional augmented with the TS<sup>surf</sup> method<sup>3</sup> for dispersion correction. We apply the repeated slab approach. Unit cell heights of 68 Å ensure vacuum heights of at least 50 Å between two consecutive slabs. Hereby a dipole correction<sup>4</sup> layers is used for decoupling.

The convergence criteria of the SCF-procedure correspond to  $1 \times 10^{-2}$  eÅ<sup>-3</sup> for the charge density,  $1 \times 10^{-5}$  eV for the energy and  $1 \times 10^{-3}$  eV Å<sup>-1</sup> for the forces.

To maximize the computational efficiency while ensuring a numerical accuracy of < 10 meV for the obtained energies, TCNE is placed on 7 copper layers in a 4x4 super cell, whose k-space is sampled with a generalized Monkhorst-Pack grid<sup>5-7</sup> (maximal spacing of  $\Delta k = \frac{2\pi}{8}$  nm<sup>-1</sup>). For the species C and N the FHI-aims default setting for a “tight” basis set are applied. The three uppermost Cu layers are computed using a “tight” species default, whereas the residual four layers employ “light” setting. In addition, both settings of Cu are slightly modified. This is well described in the supplementary information of a previous publication<sup>8</sup>, where identical DFT settings are used. It Furthermore, provides detailed information of the convergence behavior.

## 2 Favored monolayers

As predicted by Egger<sup>8</sup> et al., there are two favorable structures for different coverage ranges: For low coverages, the flat-lying structure from Figure S1 is thermodynamically the most favorable, whereas for increasing coverages the herringbone structure with upright-standing molecules (Figure S2) becomes superior.

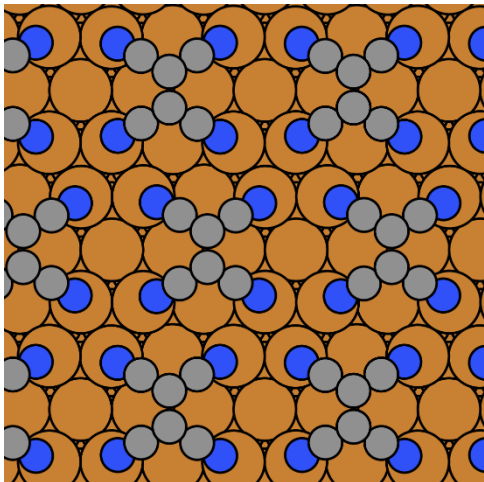


**Figure S1:** Flat-lying monolayer

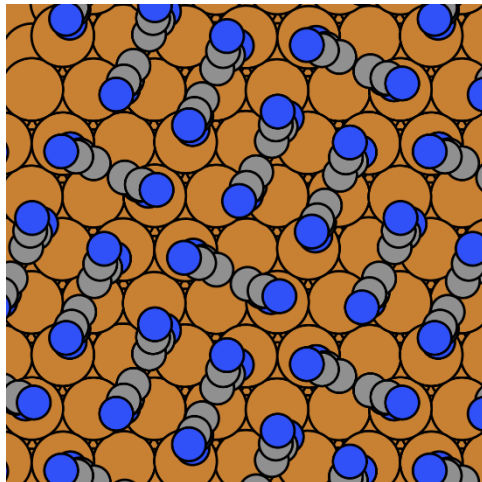


**Figure S2:** Upright-standing monolayer

### 3 Transitions

#### 3.1 $S_1 \rightarrow S_1$ transition

In Figure S3 the transition  $S_1 \rightarrow S_1$  is initialized in linear fashion. After some iterations of the nudged elastic band method, we see in Figures S4 and S5 that the central image converged towards  $S_2$ . Therefore, splits in the equivalent transitions  $S_1 \rightarrow S_2$  and  $S_2 \rightarrow S_1$ .

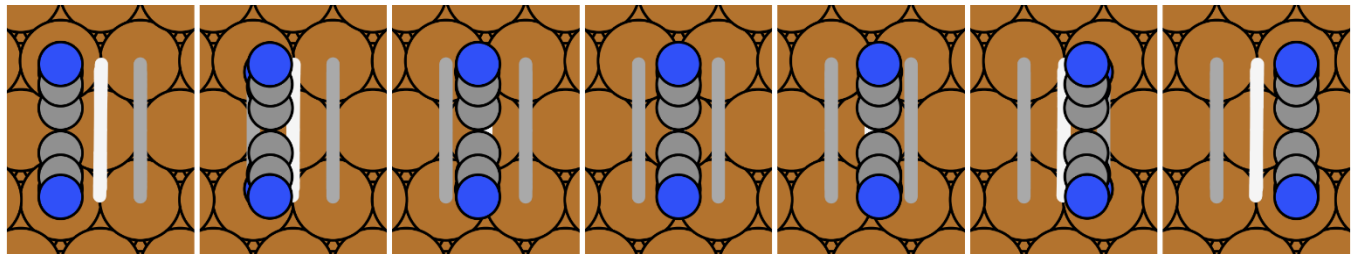


Figure S3: Initialized  $S_1 \rightarrow S_1$  transition

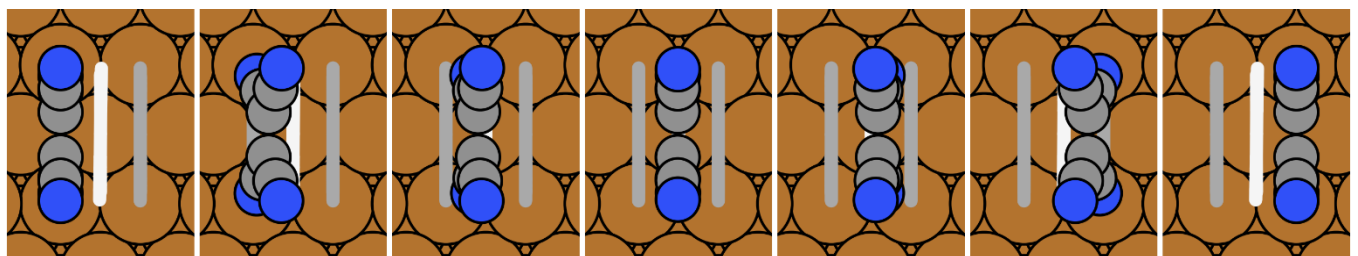


Figure S4:  $S_1 \rightarrow S_1$  transition after 74 iterations of the nudged elastic band method

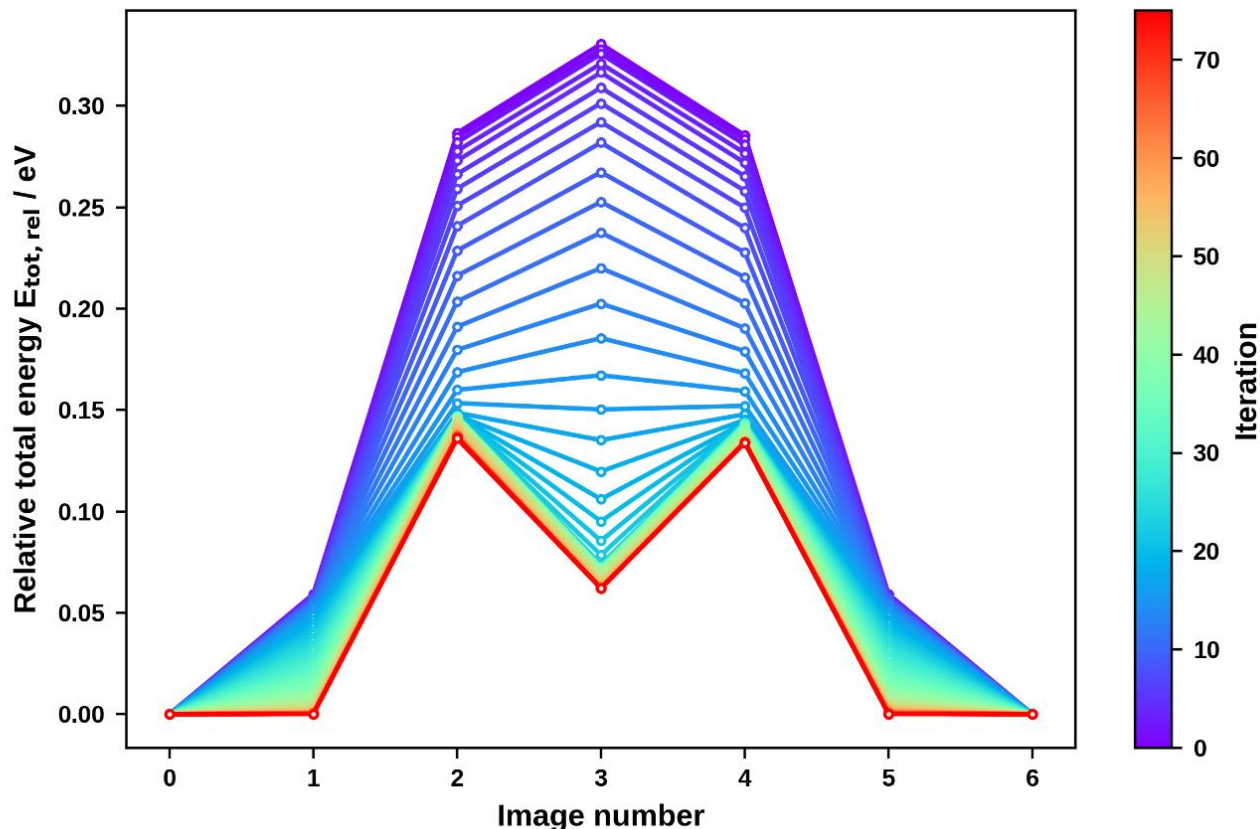
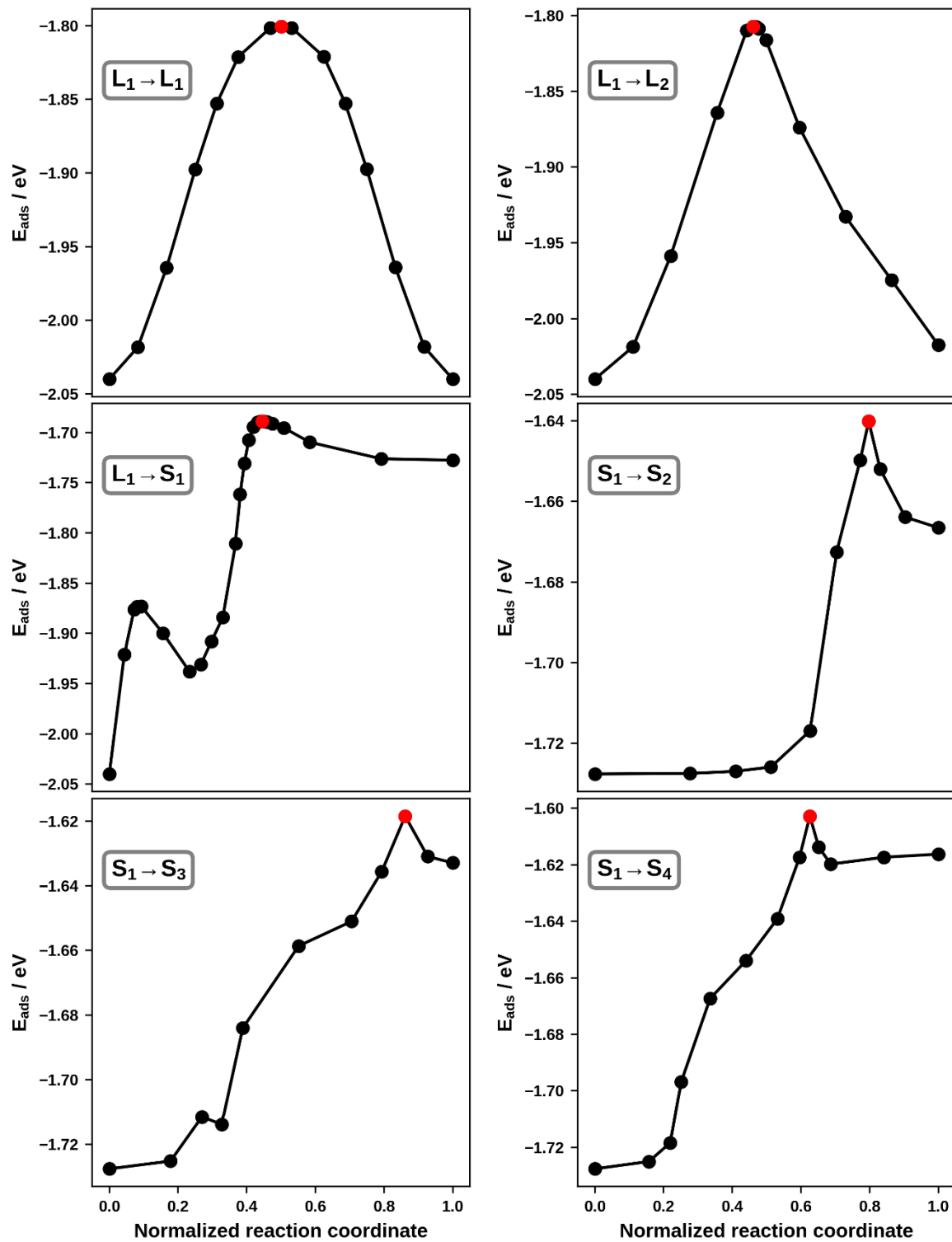


Figure S5: Energy evolution of the  $S_1 \rightarrow S_1$  transition after applying the nudged elastic band method

### 3.2 Elementary transitions

Figure S6 depicts changes in adsorption energy in dependence of the normalized reaction coordinate for all elementary transitions. Only the re-orientation  $L_1 \rightarrow S_1$  is depicted as multi-step process.



**Figure S6:** Sampled minimum energy paths described by the change of adsorption energy along the normalized reaction coordinate. Black circles show the sampled images, whereas red dots mark the obtained transition states.

## 4 Transition Rates

### 4.1 Treatment of the Gibbs free energy

We apply *ab initio* thermodynamics<sup>9</sup> to include finite temperature effects to the energies as obtained via density functional theory. For modelling growth experiments as closed systems at constant temperature and pressure, the Gibbs free energy is the relevant thermodynamic potential. In Equation 1, the Gibbs free energy of adsorption is constructed from the adsorption energy  $E_{\text{ads}}$  and the contribution of the chemical potential  $\mu_{\text{ads}}$ , while mechanical work, configuration entropy and vibration enthalpy are neglected, as it is commonly done in literature.<sup>9</sup>

$$G_{\text{ads}} = E_{\text{ads}} - \mu_{\text{ads}} N_{\text{ads}} \quad (\text{Equation 1})$$

$N_{\text{ads}}$  is the number of molecules adsorbed per unit cell, whereas  $\mu_{\text{ads}}$  is the chemical potential of the molecule in the gas phase, that depends on temperature and pressure.  $\mu_{\text{ads}}$  is obtained in the ideal gas approximation by simply using translational and rotational contributions as provided in the thermochemistry package distributed within ASE<sup>10</sup>.

For our case, all unit cells are identical and include only one adsorbate, i.e.  $N_{\text{ads}} = 1$ . Therefore,  $G_{\text{ads}}$  directly reduces to  $E_{\text{ads}}$ .

### 4.2 Elementary transitions of the re-orientation process

As only the joint processes of re-orientation are relevant for predicting process conditions for kinetically trapping the first layer of flat-lying molecules, the attempt frequencies and transition rates of the two elementary steps of the re-orientation process are not discussed in the main manuscript.

Those attempt frequencies for the elementary steps are provided in Table S1.

**Table S1:** Attempt frequencies obtained by means of harmonic transition state theory. The subscripts 1 and -1 denote forward and reverse transitions, respectively.

|                      | $L_1 \rightarrow M$  | $M \rightarrow S_1$  |
|----------------------|----------------------|----------------------|
| $A_1 / \text{Hz}$    | $1.7 \times 10^{13}$ | $5.0 \times 10^{13}$ |
| $A_{-1} / \text{Hz}$ | $9.0 \times 10^{12}$ | $8.8 \times 10^{11}$ |

In Figure S7, also the transition rates of the  $L_1 \rightarrow M$  and  $M \rightarrow S_1$  are included. Figure S8 visualizes the same content, but in a wider range.

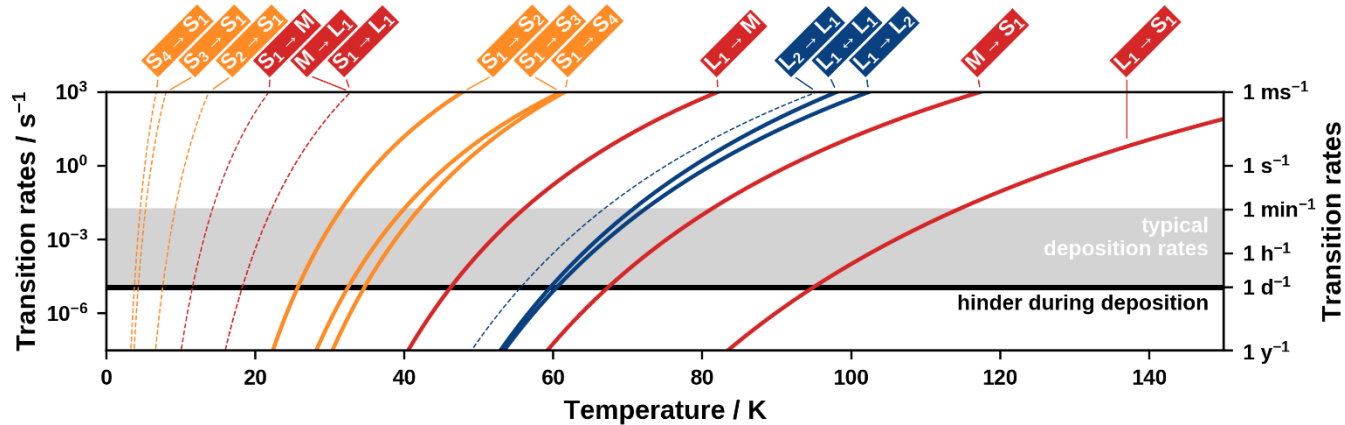


**Figure S7:** Transition rates in dependence of temperature including the two elementary transitions of the re-orientation

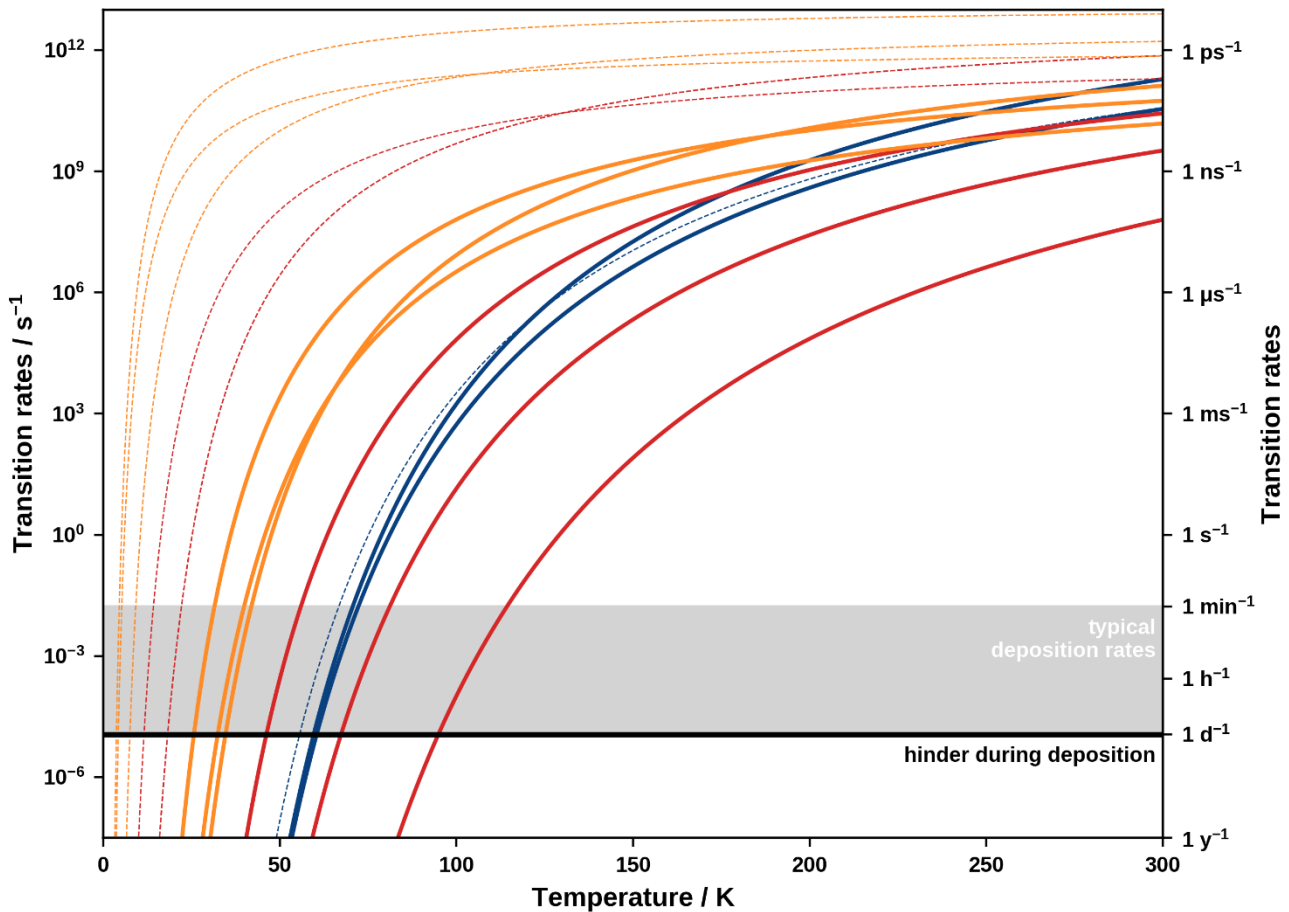


**Figure S8:** Transition rates in dependence of temperatures in an extended range (labeling according to Figure S7)

#### 4.3 Joint process of re-orientation

Since our goal is to prevent the re-orientation of individual molecules to the upright-standing position, we want to discuss a joint process of the re-orientation rather than the separate elementary processes.

For the joint process of standing-up (“ $L_1 \rightarrow S_1$ ”) the rate determining transition state is the one of step  $M \rightarrow S_1$ . This is evident in Figure S9. Thus, we assign an effective barrier of 0.35 eV to the joint process of standing-up, as indicated in Figure 5 of the main manuscript. This is constituted of the sum of the pure difference in adsorption energies of  $L_1 \rightarrow M$  (0.10 eV) and the energy barrier of  $M \rightarrow S_1$  (0.25 eV). This description is formally valid under the assumption that  $L_1$  and  $M$  are in a pre-equilibrium. In addition, the attempt frequency of  $M \rightarrow S_1$  is applied ( $5.0 \times 10^{13} \text{ s}^{-1}$ ).

For the joint process of lying down (“ $S_1 \rightarrow L_1$ ”), the rate-limiting step is  $M \rightarrow L_1$ . Therefore, rates of the joint lying-down process are obtained by employing the  $M \rightarrow L_1$  barrier of 0.06 eV and its attempt frequency ( $9.0 \times 10^{12} \text{ s}^{-1}$ ).

## 5 Uncertainty discussion

In general, there are several sources of uncertainty or errors arising from the applied DFT functional, geometric constraints, the transition state search, the transition state theory and the thermodynamic description.

Here, we discuss how these uncertainties influence the uncertainty of the temperatures that are required for suppression of single elementary or joint processes. In detail, we include the uncertainty of the transitions state and especially the influence from the vibrational frequencies.

### 5.1 Transition states and energy barriers

The quality of the obtained transition states is mainly influenced by the accuracy of the DFT calculation ( $\approx 20$  meV), as well as by the performance of the nudged elastic band method (NEB) method. In general, the geometric path used for the initialization of the NEB method can influence the resulting minimum energy path. Therefore, the path converges either to the global or only to a local solution. Checking the stability of the resulting transition paths for different initial paths is not affordable. Besides this influencing factor, the sampling resolution along the obtained path is important as well: To ensure that the highest barrier of the resulting path is captured, a plausible resolution has to be achieved. In addition, the transition state should be sampled as accurately as possible for a trustworthy measure of the energy barrier and the vibrational frequencies required for computing transition rates. Trading off the accuracy with the involved cost, we tried to push the residual NEB forces  $F_{\text{NEB}}$  on the transition state below  $0.01$  eV  $\text{\AA}^{-1}$ . The resolution of the chain of images is expressed via the maximal distance  $\Delta x$  atoms of the adsorbate exhibit between two neighbored images. For a resolution of  $\Delta x = 1$   $\text{\AA}$ , this would refer to a maximal uncertainty of the transition state energy of  $\Delta E = F_{\text{NEB}} \cdot \Delta x = 10$  meV.

In Table S2, the number of images per run, the maximal residual NEB forces of the whole chain and especially for the obtained transition state are provided, as well as the resolution at the transition state. Residual forces at the transition states below  $\approx 0.01$  eV  $\text{\AA}^{-1}$  could be obtained. The resolution at the transition state is around 0.05 to 1.00  $\text{\AA}$ . When accounting for the whole chain of images for all calculated transitions, the resolution ranges from 0.04 to 1.92  $\text{\AA}$ .

**Table S2:** Force accuracies and information about resolution of the conducted NEB runs. The number of sampled images is  $n_{\text{images}}$ . The absolute value of the maximal NEB force acting on a single atom of TCNE along the sampled transition path is denoted as  $|F|_{\text{NEB,max}}$ , whereas  $|F|_{\text{NEB,max,TS}}$  states the maximum force acting on the transition state. The resolution of the sampled images is expressed via the maximum distance atoms of the adsorbate exhibit between two neighbored images. Here,  $\Delta x_{\text{max,pre TS}}$  and  $\Delta x_{\text{max,post TS}}$  provide the resolution at the transition state.

|   | $n_{\text{images}}$ | $ F _{\text{NEB,max}} / \text{eV \AA}^{-1}$ | $ F _{\text{NEB,max,TS}} / \text{eV \AA}^{-1}$ | $\Delta x_{\text{max,pre TS}} / \text{\AA}$ | $\Delta x_{\text{max,post TS}} / \text{\AA}$ |
|---|---------------------|---|--|---|--|
| $\mathbf{L}_1 \rightarrow \mathbf{L}_1$ | 15                  | 1.8E-02                                     | 3.5E-03  | 0.10  | 0.09   |
| $\mathbf{L}_1 \rightarrow \mathbf{L}_2$ | 13                  | 3.0E-02                                     | 2.0E-03  | 0.10  | 0.05   |
| $\mathbf{L}_1 \rightarrow \mathbf{M}$   | 7                   | 1.4E-02                                     | 4.8E-03  | 0.25  | 1.00   |
| $\mathbf{M} \rightarrow \mathbf{S}_1$   | 19                  | 4.6E-02                                     | 4.3E-03  | 0.09  | 0.10   |
| $\mathbf{S}_1 \rightarrow \mathbf{S}_2$ | 11                  | 3.9E-02                                     | 1.2E-02  | 0.23  | 0.22   |
| $\mathbf{S}_1 \rightarrow \mathbf{S}_3$ | 11                  | 3.0E-02                                     | 2.7E-03  | 0.36  | 0.30   |
| $\mathbf{S}_1 \rightarrow \mathbf{S}_4$ | 13                  | 3.9E-02                                     | 6.9E-03  | 0.27  | 0.29   |

In Section 5.2.2 Figure S10 we will show that the uncertainty of the transition state energy is rather  $< 1$  meV than  $< 10$  meV. Therefore, we solely consider the  $\approx 20$  meV method error of the applied DFT functional as uncertainty of the energy barrier.

## 5.2 Vibration frequencies

For the computation of vibrational analyses at the obtained minima and transition states displacements of 0.01 Å are utilized. In addition, two corrections regarding the symmetry of the hessian and the quality of low and instable frequencies are applied as discussed in Section 5.2.1 and 5.2.2, respectively. Furthermore, relative uncertainties of vibration frequencies are estimated as well in Section 5.2.3.

### 5.2.1 Asymmetry

As Hessians are obtained in a numeric fashion, they are not ideally symmetric. Therefore, they are symmetrized. These asymmetries can be measured by calculating the root mean square value (rms) of the difference of the original and the symmetrized Hessian, as well as by the maximal absolute value of this difference (max). Accordingly, values of 0 eV Å<sup>-2</sup> refer to ideal symmetric Hessians. Tables S3 and S4 show that rms of the asymmetry ranges from 0.7 to 1.4 eV Å<sup>-2</sup>, whereas the maximal values lie between 0.1 and 0.3 eV Å<sup>-2</sup> for minima and transition states.

**Table S3:** Asymmetry of Hessian matrices for the minima.

| Minimum                  | L <sub>1</sub> | L <sub>2</sub> | M    | S <sub>1</sub> | S <sub>2</sub> | S <sub>3</sub> | S <sub>4</sub> |
|--------------------------|----------------|----------------|------|----------------|----------------|----------------|----------------|
| Rms / eV Å <sup>-2</sup> | 0.87           | 0.78           | 1.40 | 0.83           | 0.87           | 0.99           | 1.44           |
| Max / eV Å <sup>-2</sup> | 0.10           | 0.09           | 0.27 | 0.09           | 0.15           | 0.14           | 0.34           |

**Table S4:** Asymmetry of Hessian matrices of the transition states.

| Transition state         | L <sub>1</sub> → L <sub>1</sub> | L <sub>1</sub> → L <sub>2</sub> | L <sub>1</sub> → M | M → S <sub>1</sub> | L <sub>1</sub> → S <sub>1</sub> | S <sub>1</sub> → S <sub>2</sub> | S <sub>1</sub> → S <sub>3</sub> | S <sub>1</sub> → S <sub>4</sub> |
|--------------------------|---------------------------------|---------------------------------|--------------------|--------------------|---------------------------------|---------------------------------|---------------------------------|---------------------------------|
| Rms / eV Å <sup>-2</sup> | 0.71                            | 1.10                            | 1.07               | 1.07               | 1.07                            | 0.77                            | 1.23                            | 1.00                            |
| Max / eV Å <sup>-2</sup> | 0.08                            | 0.15                            | 0.16               | 0.10               | 0.10                            | 0.11                            | 0.17                            | 0.17                            |

### 5.2.2 Quality of transition states and minima

Even when the NEB run converges under the defined convergence criteria, we perform vibrational analyses to ensure that the obtained transition state is indeed a 1<sup>st</sup> order saddle point. In theory, the vibrational analysis must provide exactly one instable (negative) vibration frequency. Similarly, minima must obtain only stable (positive) vibration frequencies. But in practice, sometimes low, but positive, frequencies are erroneously identified as additional instable frequencies. This is a common issue inherent in density functional theory originating from numerical integration on a finite k-point grid.<sup>11</sup> In order to check, if the unwanted negative frequencies result from this issue or if the sampled transition state (or minimum) is a higher order saddle point, the potential energy surface is distinctly sampled along all instable vibration modes. In detail, displacements (perturbations) along these modes in the range of ± 0.1 Å are applied. The displacements are defined as the maximal displacement of the atoms in this vibration mode.

As schematically visualized in Figure S9, this easily allows then to compare the harmonically approximated vicinity of the potential energy surface along the vibration mode (as probed by the vibration analysis) with the directly calculated energy course.

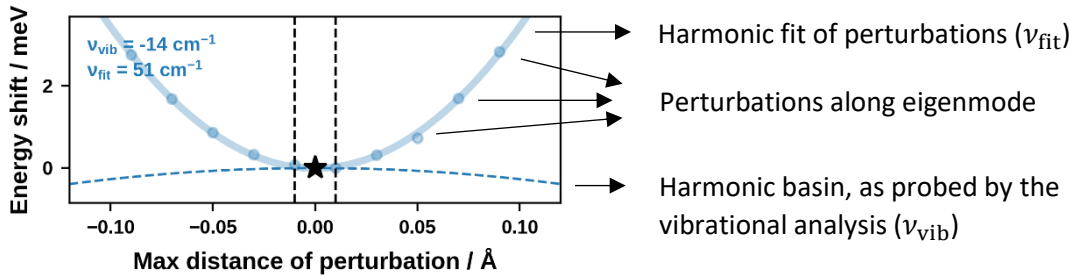


**Figure S9:** Example for an erroneously obtained instable vibration frequency.

By checking the consistency of the resulting energy course (minimum, maximum etc.) it becomes clear whether these negative modes occurred from the mentioned numerical inaccuracy or if the instable frequency correctly represents an extremum with a negative curvature. In case of the latter, the transition state search or geometry optimization must be continued and in the case of the former, we correct the eigenfrequency from the obtained perturbations by determining the curvature from fitting. This is based on the harmonic approximation of the potential energy surface  $E_{\text{harm}}$  at the point  $x_0$ , that is either an obtained transition state or a minimum.  $\vec{H}$  is the hessian and  $\vec{M}$  the reduced mass matrix. For small deviations along an eigenmode  $j$  ( $x_0 + a\vec{u}_j$ ), this reduces to:

$$E_{\text{harm}}(x_0 + a\vec{u}_j) = E(x_0) + \frac{1}{2}a^2\vec{u}_j^T \vec{H} \vec{u}_j \quad (\text{Equation 2})$$

$$E_{\text{harm}}(x_0 + a\vec{u}_j) = E(x_0) + \frac{1}{2}a^2\vec{u}_j^T \vec{M}^{-1}(\vec{M}\vec{H}) \vec{u}_j \quad (\text{Equation 3})$$

$$E_{\text{harm}}(x_0 + a\vec{u}_j) = E(x_0) + \frac{1}{2}a^2\vec{u}_j^T \vec{M}^{-1}\omega_j^2 \vec{u}_j \quad (\text{Equation 4})$$

$$E_{\text{harm}}(a) = E(x_0) + \frac{1}{2}c_j a^2 \quad \text{with } c_j = \omega_j^2 m_j \quad \text{and } m_j = \vec{u}_j^T \vec{M}^{-1} \vec{u}_j \quad (\text{Equation 5})$$

This now enables translating the curvature  $c_{j,\text{fit}}$  of the perturbed data (force constant) into a vibration frequency via  $\omega_{j,\text{fit}} = \sqrt{c_{j,\text{fit}}/m_j} = 2\pi\nu_{j,\text{fit}}$ .

Figure S10 visualizes the results of this approach for all instable modes of minima and transition states. Three of the calculated transition states exhibit an additional instable mode. Also, for three of the minima one instable frequency was found. But when comparing the curvatures from the vibrational analyses with the distinct perturbations along the instable modes, we identify all additional instable vibration frequencies to result from numerical inaccuracies. By harmonically fitting the energies of the perturbed points all obtained vibration frequencies were corrected.

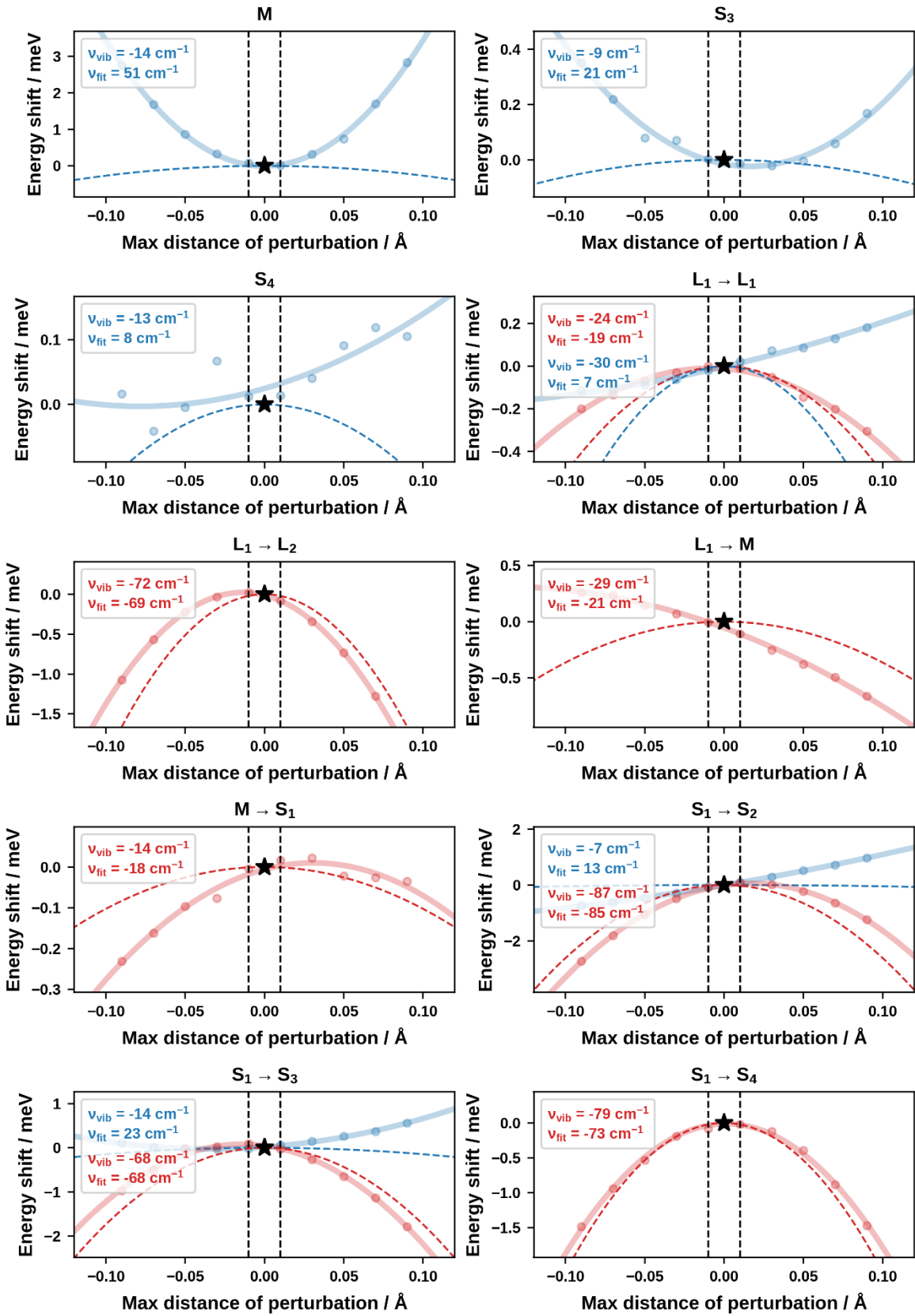


**Figure S10:** Displacements along all unstable vibration modes appearing at minima and states. A schematic description of the content is provided in Figure S9.

### 5.2.3 Uncertainty estimation of vibrational frequencies

The uncertainty estimation of the computed vibrational frequencies depends also the quality of the obtained extremum. For the case that the computed extremum lies within the harmonic range of the real extremum, the curvatures and vibration frequencies should be constant. In practice, numerical instabilities, which are caused by DFT, can additionally distort vibration frequencies (for details see Section 5.2.2).

To get a rough estimate of the uncertainty of vibrational frequencies, the process described in the previous section was repeated for six eigenmodes with frequencies from 11 to  $2218\text{ cm}^{-1}$ , as displayed in Figure S11. This was done for the rate-limiting transition state of the joint process of standing up ( $\text{L}_1 \rightarrow \text{S}_1$ ).

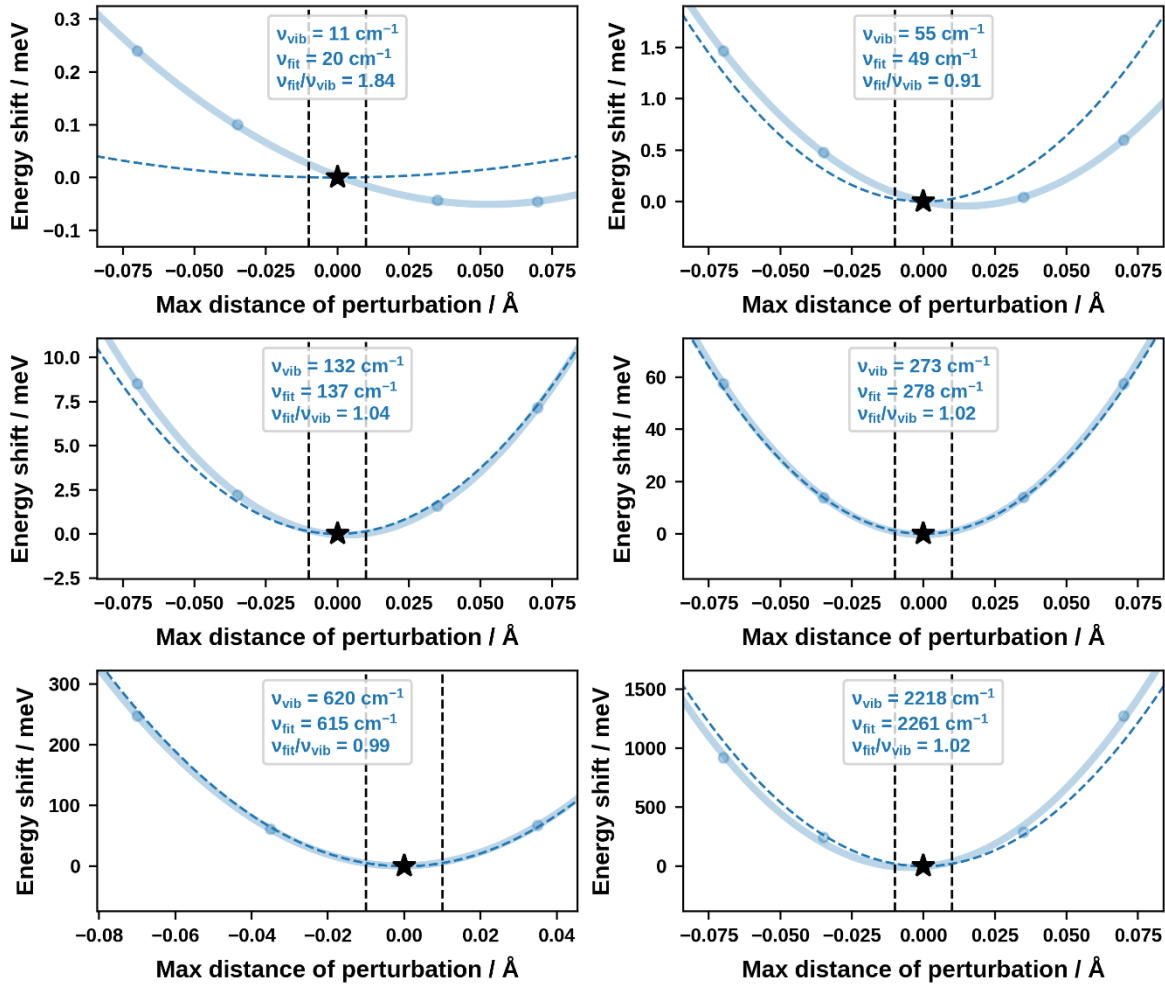


**Figure S11:** Perturbations along different vibration modes of the rate-limiting transition state of  $\text{L}_1 \rightarrow \text{S}_1$ . A schematic description of the content is provided in Figure S9.

### 5.3 Attempt frequencies

The attempt frequency  $A$  is obtained via the stable frequencies of the initial ( $\nu_i^{\text{ini}}$ ) and the transition state ( $\nu_i^{\text{TS}}$ ), as stated in Equation 6. The ansatz and the result of the relative uncertainty are given by Equation 7 and 8, respectively.

$$A = \frac{\prod_{i=1}^{3N} \nu_i^{\text{ini}}}{\prod_{i=1}^{3N-1} \nu_i^{\text{TS}}} = \frac{P^{\text{ini}}}{P^{\text{TS}}} \quad \text{with } P = \prod_i \nu_i \quad (\text{Equation 6})$$

$$\Delta A = \sqrt{\left(\frac{\partial A}{\partial P^{\text{ini}}}\right)^2 \cdot (\Delta P^{\text{ini}})^2 + \left(\frac{\partial A}{\partial P^{\text{TS}}}\right)^2 \cdot (\Delta P^{\text{TS}})^2} \quad \text{with } \frac{\Delta P}{P} = \sqrt{\sum_i \left(\frac{\Delta \nu_i}{\nu_i}\right)^2} \quad (\text{Equation 7})$$

$$\frac{\Delta A}{A} = \sqrt{\sum_{i=1}^{3N} \left(\frac{\Delta \nu_i^{\text{ini}}}{\nu_i^{\text{ini}}}\right)^2 + \sum_{i=1}^{3N-1} \left(\frac{\Delta \nu_i^{\text{TS}}}{\nu_i^{\text{TS}}}\right)^2} \quad (\text{Equation 8})$$

The relative uncertainty of the attempt frequency solely depends on the relative uncertainties of the computed vibration frequencies. Based on the results of Figure S11, we estimate the relative uncertainty of the attempt frequencies to  $\frac{\Delta A}{A} \approx 10$ .

### 5.4 Suppression temperatures

In the main paper temperatures  $T_{\text{supp}}$  are proposed that sufficiently suppress transitions of individual molecules. In detail, the temperatures  $T_{\text{supp}}$  are determined for transition rates of  $k_{\text{supp}} = 1 \text{ s}^{-1}$  via Equation 9 (energy barrier  $\Delta E^\ddagger$ , the attempt frequency  $A$ ).

$$T_{\text{supp}} = \frac{\Delta E^\ddagger}{k_B (\ln(A) - \ln(k_{\text{supp}}))} \quad (\text{Equation 9})$$

To get a rough feeling for the uncertainties of the suppression temperatures we perform a simple error propagation. The general approach and the resulting description are shown in Equations 10 and 11, respectively.

$$\Delta T_{\text{supp}} = \sqrt{\left(\frac{\partial T_{\text{supp}}}{\partial \Delta E^\ddagger}\right)^2 \cdot (\Delta \Delta E^\ddagger)^2 + \left(\frac{\partial T_{\text{supp}}}{\partial A}\right)^2 \cdot (\Delta A)^2 + \left(\frac{\partial T_{\text{supp}}}{\partial k_{\text{supp}}}\right)^2 \cdot (\Delta k_{\text{supp}})^2} \quad (\text{Equation 10})$$

$$\Delta T_{\text{supp}} = T_{\text{supp}} \cdot \sqrt{\left(\frac{\Delta \Delta E^\ddagger}{\Delta E^\ddagger}\right)^2 + \left(\frac{1}{\ln(A) - \ln(k_{\text{supp}})} \cdot \frac{\Delta A}{A}\right)^2 + \left(\frac{1}{\ln(A) - \ln(k_{\text{supp}})} \cdot \frac{\Delta k_{\text{supp}}}{k_{\text{supp}}}\right)^2} \quad (\text{Equation 11})$$

In Equation 11, it is evident that the uncertainty of the suppression temperatures grows with its nominal value. For all transitions  $\Delta \Delta E^\ddagger = 0.02 \text{ eV}$  is assumed, what corresponds to the method error of DFT, and a relative error of one order of magnitude for  $A$ , i.e.  $\frac{\Delta A}{A} = 10$  (for more details see Section 5.3).  $\Delta k_{\text{supp}}$  is not accounted ( $\Delta k_{\text{supp}} = 0$ ).

The results for the forward and reverse transitions are visualized in Figure S12 and stated in Table S5 and S6, respectively. Therein, the nominal values ( $T_{\text{supp}}$ ) and the uncertainty estimate ( $\Delta T_{\text{supp}}$ ) of the suppression temperature are stated, as well as the single uncertainty contributions regarding the attempt frequency and the energy barrier.

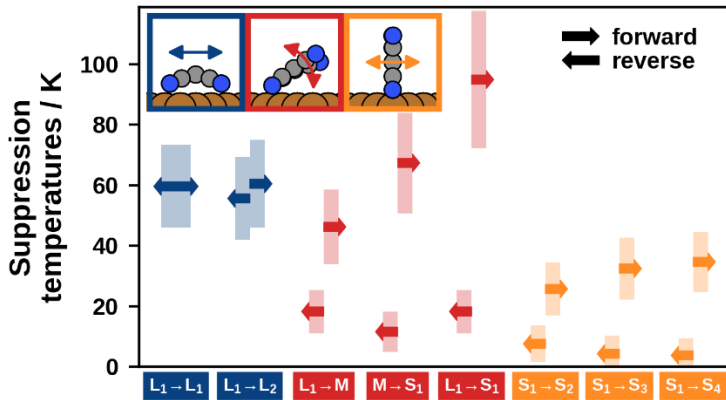


**Figure S12:** Estimated temperatures for suppression obtained for transition rates of 1 day<sup>-1</sup>. The arrow directions indicate the suppression temperatures required for forward or reverse transitions. Shaded areas indicate the temperature uncertainties connected to the respective transition.

**Table S5:** Uncertainties of suppression temperatures of forward transitions

| Transition                          | $T_{\text{supp}} / \text{K}$ | $\Delta T_{\text{supp}} / \text{K}$ | $\left  \frac{\partial T_{\text{supp}}}{\partial A} \cdot \Delta A \right  / \text{K}$ | $\left  \frac{\partial T_{\text{supp}}}{\partial \Delta E^\ddagger} \cdot \Delta \Delta E^\ddagger \right  / \text{K}$ |
|-------------------------------------|------------------------------|-------------------------------------|--|--|
| $\text{L}_1 \rightarrow \text{L}_1$ | 60                           | 14                                  | 13   | 5  |
| $\text{L}_1 \rightarrow \text{L}_2$ | 60                           | 15                                  | 14   | 5  |
| $\text{L}_1 \rightarrow \text{M}$   | 46                           | 12                                  | 11   | 6  |
| $\text{M} \rightarrow \text{S}_1$   | 67                           | 17                                  | 16   | 5  |
| $\text{L}_1 \rightarrow \text{S}_1$ | 95                           | 23                                  | 22   | 5  |
| $\text{S}_1 \rightarrow \text{S}_2$ | 26                           | 9                                   | 7  | 6  |
| $\text{S}_1 \rightarrow \text{S}_3$ | 32                           | 10                                  | 8  | 6  |
| $\text{S}_1 \rightarrow \text{S}_4$ | 35                           | 10                                  | 8  | 6  |

**Table S6:** Uncertainties of suppression temperatures of reverse transitions

| Transition                          | $T_{\text{supp}} / \text{K}$ | $\Delta T_{\text{supp}} / \text{K}$ | $\left  \frac{\partial T_{\text{supp}}}{\partial A} \cdot \Delta A \right  / \text{K}$ | $\left  \frac{\partial T_{\text{supp}}}{\partial \Delta E^\ddagger} \cdot \Delta \Delta E^\ddagger \right  / \text{K}$ |
|-------------------------------------|------------------------------|-------------------------------------|--|--|
| $\text{L}_1 \rightarrow \text{L}_1$ | 60                           | 14                                  | 13   | 5  |
| $\text{L}_2 \rightarrow \text{L}_1$ | 56                           | 14                                  | 13   | 5  |
| $\text{M} \rightarrow \text{L}_1$   | 18                           | 7                                   | 4  | 6  |
| $\text{S}_1 \rightarrow \text{M}$   | 12                           | 7                                   | 3  | 6  |
| $\text{S}_1 \rightarrow \text{L}_1$ | 18                           | 7                                   | 4  | 6  |
| $\text{S}_2 \rightarrow \text{S}_1$ | 8                            | 6                                   | 2  | 6  |
| $\text{S}_3 \rightarrow \text{S}_1$ | 4                            | 6                                   | 1  | 6  |
| $\text{S}_4 \rightarrow \text{S}_1$ | 4                            | 6                                   | 1  | 6  |

## 6 References

- (1) Blum, V.; Gehrke, R.; Hanke, F.; Havu, P.; Havu, V.; Ren, X.; Reuter, K.; Scheffler, M. Ab Initio Molecular Simulations with Numeric Atom-Centered Orbitals. *Comput. Phys. Commun.* **2009**, *180* (11), 2175–2196. <https://doi.org/10.1016/j.cpc.2009.06.022>.
- (2) Perdew, J. P.; Burke, K.; Ernzerhof, M. Generalized Gradient Approximation Made Simple. *Phys. Rev. Lett.* **1996**, *77* (18), 3865–3868. <https://doi.org/10.1103/PhysRevLett.77.3865>.
- (3) Tkatchenko, A.; Scheffler, M. Accurate Molecular van Der Waals Interactions from Ground-State Electron Density and Free-Atom Reference Data. *Phys. Rev. Lett.* **2009**, *102* (7), 073005. <https://doi.org/10.1103/PhysRevLett.102.073005>.
- (4) Neugebauer, J.; Scheffler, M. Adsorbate-Substrate and Adsorbate-Adsorbate Interactions of Na and K Adlayers on Al(111). *Phys. Rev. B* **1992**, *46* (24), 16067–16080. <https://doi.org/10.1103/PhysRevB.46.16067>.
- (5) Moreno, J.; Soler, J. M. Optimal Meshes for Integrals in Real- and Reciprocal-Space Unit Cells. *Phys. Rev. B* **1992**, *45* (24), 13891–13898. <https://doi.org/10.1103/PhysRevB.45.13891>.
- (6) Monkhorst, H. J.; Pack, J. D. Special Points for Brillouin-Zone Integrations. *Phys. Rev. B* **1976**, *13* (12), 5188–5192. <https://doi.org/10.1103/PhysRevB.13.5188>.
- (7) Wisesa, P.; McGill, K. A.; Mueller, T. Efficient Generation of Generalized Monkhorst-Pack Grids through the Use of Informatics. *Phys. Rev. B* **2016**, *93* (15), 155109. <https://doi.org/10.1103/PhysRevB.93.155109>.
- (8) Egger, A. T.; Hörmann, L.; Jeindl, A.; Scherbela, M.; Obersteiner, V.; Todorović, M.; Rinke, P.; Hofmann, O. T. Charge Transfer into Organic Thin Films: A Deeper Insight through Machine-Learning-Assisted Structure Search. *Adv. Sci.* **2020**, *7* (15), 2000992. <https://doi.org/10.1002/advs.202000992>.
- (9) Reuter, K.; Scheffler, M. Composition, Structure, and Stability of RuO<sub>2</sub>(110) as a Function of Oxygen Pressure. *Phys. Rev. B* **2001**, *65* (3), 035406. <https://doi.org/10.1103/PhysRevB.65.035406>.
- (10) Hjorth Larsen, A.; JØrgen Mortensen, J.; Blomqvist, J.; Castelli, I. E.; Christensen, R.; Dułak, M.; Friis, J.; Groves, M. N.; Hammer, B.; Hargus, C.; Hermes, E. D.; Jennings, P. C.; Bjerre Jensen, P.; Kermode, J.; Kitchin, J. R.; Leonhard Kolsbjerg, E.; Kubal, J.; Kaasbjerg, K.; Lysgaard, S.; Bergmann Maronsson, J.; Maxson, T.; Olsen, T.; Pastewka, L.; Peterson, A.; Rostgaard, C.; SchiØtz, J.; Schütt, O.; Strange, M.; Thygesen, K. S.; Vegge, T.; Vilhelmsen, L.; Walter, M.; Zeng, Z.; Jacobsen, K. W. The Atomic Simulation Environment - A Python Library for Working with Atoms. *Journal of Physics Condensed Matter*. Institute of Physics Publishing June 7, 2017, p 30. <https://doi.org/10.1088/1361-648X/aa680e>.
- (11) Ochterski, J. W. *Vibrational Analysis in Gaussian*.